https://doi.org/10.5194/egusphere-2026-6332
Preprint. Discussion started: 4 November 2026
© Author(s) 2026. CC BY 4.0 License.

Quantifying turbulent kinetic energy in the middle atmosphere from wind and temperature observations: a method validated against a global model

Nikita Goswami[1], Irina Strelnikova[1], Robin Wing[1], Tridib Banerjee[2], Yanmichel A. Morfa[1], Aditya Baksi[1], Ulrich Achatz[2], and Gerd Baumgarten[1]

[1]Leibniz Institute of Atmospheric Physics at the University of Rostock, Kühlungsborn, Germany
[2]Institute for Atmospheric and Environmental Sciences, Goethe University Frankfurt, Frankfurt, Germany

Correspondence: Nikita Goswami (goswami@iap-kborn.de)

Abstract.

Quantifying middle-atmosphere turbulence from observational data remains a major challenge. While ground-based lidars have accumulated decades of high-resolution wind and temperature profiles, extracting a quantitative turbulence metric from them has not been possible, forcing observers to rely on ambiguous proxies like the Richardson number (Ri). However, using the UA-ICON model, we first demonstrate that Ri alone is an insufficient indicator of turbulence intensity. To overcome this limitation, we present an algorithm that extracts turbulent kinetic energy (TKE) directly from observational data by adapting the prognostic TKE budget of the ICOsahedral Non-hydrostatic (ICON) general circulation model to work exclusively with observable variables. Validated against UA-ICON output, our algorithm reconstructs TKE from wind and temperature fields without tuning, matching the model TKE with a correlation of 0.98. Applying this method to 187 hours of ALOMAR RMR lidar measurements, we obtain the first quantitative estimate of TKE in the 35 to 60 km altitude range derived entirely from lidar observations. The results reveal turbulence as highly structured, intermittent patches with a minimum of $0.09\ \mathrm{m^2\ s^{-2}}$ and a maximum of $2.8\ \mathrm{m^2\ s^{-2}}$ (1st–99th percentile) and a median of $0.54\ \mathrm{m^2\ s^{-2}}$. By aligning observations with model parameterisations, this approach unlocks the potential of the long-term observational record for the quantitative study of middle-atmosphere turbulence.

1 Introduction

1.1 Atmospheric Turbulence

Turbulence refers to chaotic, irregular fluid motions that arise when atmospheric flow becomes unstable (Stull, 1988). This instability arises through two mechanisms. In dynamic instability, strong vertical wind shear overcomes buoyancy's stabilising effect, and the flow breaks down into disordered eddies (Stull, 1988). In convective instability, steep temperature gradients make the atmosphere statically unstable, which drives overturning and mixing (Stull, 1988). In both cases, organised flow gives way to chaotic small-scale motions that occur in intermittent patches, which can subsequently be modified through stability and shear into thin layers that vary strongly in space and time (Lübken, 1997; Strelnikov et al., 2017). Energy then cascades down

https://doi.org/10.5194/egusphere-2026-6332
Preprint. Discussion started: 4 November 2026
© Author(s) 2026. CC BY 4.0 License.

to smaller and smaller scales until it is finally dissipated as heat (Richardson, 1920; Kolmogorov, 1941). This mixing transports momentum, heat, and chemical constituents between atmospheric layers (Stull, 1988; Hocking, 1999), and in the stratosphere and mesosphere it shapes the thermal structure, the distribution of trace gases, and the momentum budget that drives the large-scale circulation (Fritts and Alexander, 2003; Holton and Hakim, 2013). Turbulence in the upper atmosphere is difficult to study because it occurs in thin, intermittent, and patchy layers. Furthermore, these turbulent motions have small, non-periodic amplitudes and occur at spatial scales that often fall below instrument resolution.

1.2 Turbulence Measurement and Estimation

Turbulence can be measured or estimated in different ways, either through observations with instruments or through simulation by atmospheric models. Turbulence observations can be divided into two different techniques: in-situ techniques, which sample the atmosphere directly, and remote sensing techniques, which observe turbulence from the ground. Both techniques estimate the turbulent energy dissipation rate (ε), the rate at which energy is dissipated by turbulent motions, which is one of the key measures of turbulence intensity. Each, however, is restricted in altitude, duration, or coverage, so continuous or climatological monitoring is difficult to achieve (Strelnikov et al., 2017).

The most direct way to measure turbulence is with in-situ techniques, such as rockets, radiosondes, aircraft, and flux towers, which resolve structure down to very small scales (Lübken, 1997; Strelnikov et al., 2003; Ko et al., 2024; Söder et al., 2021; MacCready Jr, 1964; Sharman et al., 2014; Kaimal and Finnigan, 1994; Nilsson et al., 2016). In contrast, remote sensing techniques, such as ground-based mesosphere-stratosphere-troposphere (MST) radars, enable long-term climatological studies through their continuous operation from a fixed location (Woodman and Guillen, 1974; Hocking, 1985; Nastrom and Eaton, 1997), but they have their own limitations (Hocking, 1985; Dehghan and Hocking, 2011). However, lidar has also been used to measure turbulence (Xian et al., 2025), though this work has focused mostly on the boundary layer and troposphere.

On the other hand, atmospheric models also estimate turbulence, but in a different term: turbulent kinetic energy (TKE), the kinetic energy associated with turbulent motions. TKE and (ε) represent physically distinct quantities and cannot be directly compared one-to-one. Models like ICON (Raschendorfer, 2001; Doms et al., 2021) and WRF (Nakanishi and Niino, 2009) generally compute TKE using a prognostic equation based on the Mellor–Yamada closure (Mellor and Yamada, 1974, 1982), though the specific implementation of the scheme differs by model. These approaches have been used for decades, with WRF's scheme applied within the boundary layer (Kumar et al., 2021), while ICON's implementation extends from the boundary layer up into the upper atmosphere (Banerjee et al., 2026). Table B1 summarises observational studies using different turbulence measurement methods, while Table B2 summarises modelling studies that compute TKE.

1.3 Objectives

Over the past several decades, researchers have collected wind and temperature data in the middle atmosphere using ground-based instruments. Some of the main long-term facilities include the Rayleigh-Mie-Raman (RMR) lidar series at the Observatoire de Haute-Provence in France, operating since the late 1970s (Keckhut et al., 1993; Wing et al., 2018) for temperature and campaign-based wind observations since the late 1980s. Similarly, the ALOMAR RMR lidar in northern Norway has operated

https://doi.org/10.5194/egusphere-2026-6332
Preprint. Discussion started: 4 November 2026
© Author(s) 2026. CC BY 4.0 License.

continuously since 1994 (von Zahn et al., 2000; Fiedler and Baumgarten, 2024), later adding the capability to routinely measure winds (Baumgarten, 2010). Further, the RMR lidar at Kühlungsborn, Germany, has measured temperatures since 2010 (Gerding et al., 2016) and incorporated regular wind observations since 2021 (Gerding et al., 2024).

Despite this wealth of data, no established method exists for extracting a turbulence quantity from wind and temperature profiles alone in the middle atmosphere. Observers have instead relied on the gradient Richardson number (Ri), a ratio of buoyancy to wind shear, is a proxy for turbulence (Richardson, 1920), and it has been used widely across observational studies (Ratnam et al., 2002; Fritts and Alexander, 2003; Shao et al., 2023; Sherman and She, 2006; Liu, 2007; Andrioli et al., 2017; Schneider et al., 2017; Wing et al., 2025). For instance, Yang and Liu (2022) recently demonstrated the utility of simultaneous lidar measurements by using Ri to successfully map the occurrence of dynamic and convective instabilities in the mesopause region. However, direct comparisons with measured turbulence show that Ri is an ambiguous estimator for turbulence: a single value of Ri can correspond to very different turbulence intensities (Haack et al., 2014; Grachev et al., 2013). This ambiguity motivates the need for a method that quantifies TKE directly, rather than relying on Ri as a proxy.

Most turbulence measurements exist in the troposphere or the mesopause region; the 35-60 km range remains largely unexplored (Table B1). Since instruments and models express turbulence in different quantities (Tables B1 and B2), this raises the central question of the study: can an algorithm apply the same physical prognostic TKE framework used by models to observational wind and temperature observations in the stratosphere and lower mesosphere, and estimate TKE consistently with the model-based approach? We address this by first developing and validating the algorithm using wind and temperature fields from UA-ICON, for which the model TKE is available as a reference; once validated, the same algorithm is applied to real lidar observations, providing a quantitative estimate of TKE in the middle atmosphere (35–60 km) derived entirely from lidar measurements. The following sections present the data (Sect. 2) and methodology (Sect. 3), followed by the results (Sect. 4), a discussion (Sect. 6), and a summary of the main findings and conclusions (Sect. 7).

2 Data

2.1 Model Run

We ran simulations using the Icosahedral Nonhydrostatic Climate & Weather Forecasting Model ICON (Zängl et al., 2015, public ICON release 2025.10-1) with upper-atmospheric extension (UA-ICON Borchert et al., 2019) on a triangular C grid R02B04 with a nominal horizontal grid spacing of approximately 160 km. The model had 120 vertical levels with a maximum thickness of 700 m below 40 km. The model top was at 150 km with a sponge layer starting from 110 km. The simulations were one-day runs initialised with IFS analysis (00:00 UTC November 1, 1991) up to 60 km, along with additional blended upper-atmosphere climatology (see Borchert et al. (2019) appendix) with no warm-up since ICON already estimates the initial turbulence from the initialised fields. All experiments used subgrid-scale parameterisations from the standard ICON-NWP physics package, including the turbulence scheme Raschendorfer (2001), and ran with 60 s time steps, with model fields output at hourly resolution for the present analysis.

https://doi.org/10.5194/egusphere-2026-6332
Preprint. Discussion started: 4 November 2026
© Author(s) 2026. CC BY 4.0 License.

Regarding the model run and turbulence handling, note the following additional details. First, although ICON public release currently ships with a more advanced gravity wave parameterisation in MSGWaM, presented in Voelker et al. (2024), the model runs for this paper instead use their traditional gravity-wave drag scheme (Orr et al., 2010, non-orographic) and (Lott and Miller, 1997, orographic). Consequently, we also did not use explicit bidirectional turbulence coupling between the gravity and turbulence schemes, as has been demonstrated in UA-ICON with MSGWaM recently by Banerjee et al. (2026). Furthermore, although the manuscript closely follows ICON's turbulence handling, differences remain. Namely, the initial TKE is computed differently, primarily due to the initial mixing-length scale guesses and a non-iterative initial solution (as opposed to what is described below). Additionally, the theory below omits variations in the diagnosis of TKE (velocity scale) tendency that arise from additional steps like floors, temporal substeps, limiters, conditional extra diffusion, and other numerical operations in ICON that are driven more by computational requirements than by model physics.

2.2 Observation Data (Lidar)

The observations were made with the ALOMAR Doppler Rayleigh–Mie–Raman (RMR) lidar in Northern Norway (69.28°N, 16.01°E), which measures wind and temperature simultaneously in the middle atmosphere, both day and night. Full technical and instrumental details can be found in Baumgarten (2010); Fiedler and Baumgarten (2024). As a test case, we use a continuous observation period from 3 February 2017 at 06:00 UTC to 10 February 2017 at 13:00 UTC, spanning 187 h (about 7.8 days) (Rüfenacht et al., 2018). We make use of wind and temperature profiles retrieved over 35–60 km at a native vertical resolution of 150 m and a temporal resolution of 5 min. Outliers and spikes are removed from the wind and temperature fields before the analysis.

3 Methodology

3.1 The Richardson Number

The Richardson Number (Ri) is a dimensionless ratio of buoyancy to wind shear, first introduced by Richardson (1920) and defined as (Stull, 1988; Holton and Hakim, 2013):

$$Ri = \frac{N^2}{S^2} = \frac{\frac{g}{\theta}\frac{\partial \theta}{\partial z}}{\left(\frac{\partial u}{\partial z}\right)^2 + \left(\frac{\partial v}{\partial z}\right)^2} \tag{1}$$

where g is gravitational acceleration, θ is the potential temperature, z is altitude, and u and v are the horizontal wind components. The numerator, N^2, is the Brunt-Väisälä frequency squared, which describes how strongly the atmosphere resists vertical motion due to thermal stratification. The denominator, S^2, is the square of the vertical wind shear, which quantifies how strongly the wind changes with altitude. For the lidar, where temperature is measured directly, N^2 is evaluated from the temperature profile and the adiabatic lapse rate,

$$N^2 = \frac{g}{T}\left(\frac{\partial T}{\partial z} + \frac{g}{c_p}\right), \tag{2}$$

https://doi.org/10.5194/egusphere-2026-6332
Preprint. Discussion started: 4 November 2026
© Author(s) 2026. CC BY 4.0 License.

where T is temperature and c_p is the specific heat of air at constant pressure. In a strongly stratified atmosphere, buoyancy dominates, Ri is large, and turbulence is suppressed. Where the shear is strong enough to overcome buoyancy, Ri becomes small, and the flow becomes susceptible to instability. Miles (1961) and Howard (1961) showed through linear stability analysis that a stratified shear flow is stable to small perturbations as long as Ri ≥ 0.25 everywhere, giving the classical stability criterion:

$$Ri < 0.25 \longrightarrow \text{turbulence likely}$$
$$0.25 < Ri < 1 \longrightarrow \text{transition zone}$$
$$Ri > 1 \longrightarrow \text{flow is stable}$$

The criterion is one-directional: Ri above 1 suggests stability, whereas Ri below 0.25 only points towards the possibility of instability, and the flow may or may not become turbulent. Direct comparisons with measured turbulence have repeatedly shown Ri to be an insufficient indicator of turbulence intensity (Haack et al., 2014; Grachev et al., 2013), a limitation we explicitly demonstrate using UA-ICON in Sect. 4.

3.2 The TKE Budget Equation

Turbulent Kinetic Energy (TKE) is the kinetic energy carried by turbulent motions in the atmosphere. Atmospheric flow is never perfectly laminar: the wind at any point contains small random fluctuations superimposed on the mean flow. Those fluctuations are the turbulent motions, and TKE is the energy stored in them. It is defined as half the sum of the squared velocity fluctuations in all three directions (Stull, 1988; Holton and Hakim, 2013) and denoted by e:

$$\overline{e} = \frac{1}{2}\overline{(u'^2 + v'^2 + w'^2)} \tag{3}$$

where u', v', and w' are the fluctuating parts of the wind in the zonal, meridional, and vertical directions, and the overbar denotes a time average that is sufficiently small to remove background motion and perturbations due to gravity waves. Each component represents a different direction of turbulent motion. The horizontal components, u'^2 and v'^2, contain the energy in the east-west and north-south fluctuations, which primarily arise from wind shear: as the wind changes speed or direction with altitude, the resulting instabilities feed energy into horizontal turbulent motions. The vertical component, w'^2, captures the up-and-down motions, which do most of the work of mixing heat, momentum, and chemical constituents between atmospheric layers (Holton and Hakim, 2013; Fritts and Alexander, 2003).

In the middle and upper atmosphere, the turbulent length scales are far smaller than the resolution of lidar wind and temperature profiles, so Eq. 3 cannot be evaluated directly from these measurements. TKE must instead be obtained through the full prognostic budget equation described below. The goal of this study is to estimate TKE directly from wind and temperature observations, giving quantitative values of turbulent energy.

https://doi.org/10.5194/egusphere-2026-6332
Preprint. Discussion started: 4 November 2026
© Author(s) 2026. CC BY 4.0 License.

Building on the turbulence concepts of Kolmogorov (1941) and Prandtl (1945), the TKE budget equation was formulated and adapted for atmospheric modelling by Mellor and Yamada (1974) and Mellor and Yamada (1982):

$$\frac{\partial \overline{e}}{\partial t} = \underbrace{K_m S_V^2}_{\text{Shear Production}} \underbrace{- K_h N^2}_{\text{Buoyancy}} \underbrace{- c\frac{\overline{e}^{3/2}}{l_{\text{diss}}}}_{\text{Dissipation}} \underbrace{+ \frac{\partial}{\partial z}\left(K_e \frac{\partial \overline{e}}{\partial z}\right)}_{\text{Vertical Diffusion}} \tag{4}$$

where $\overline{e}$ is the TKE defined in Eq. 3. This budget equation governs how TKE evolves in the atmosphere, accounting for the processes that produce, destroy, and transport TKE at any given point. The left-hand side is the rate of change of TKE with time, and the right-hand side contains four terms, each a different physical process:

- The first term, $K_m S_V^2$, is shear production. Large changes in wind speed or direction with altitude create mechanical instabilities that generate turbulence, and the stronger the shear S_V^2, the more TKE is produced. The coefficient K_m is the turbulent exchange coefficient for momentum, which sets how efficiently shear is converted into turbulent energy (Stull, 1988; Mellor and Yamada, 1974).

- The second term, $K_h N^2$, is the buoyancy term, which either suppresses or generates TKE depending on the thermal stratification. N^2 is the Brunt-Väisälä frequency squared, a measure of static stability. Under stable conditions ($N^2 > 0$), turbulent motions must work against gravity to displace air parcels vertically; thus, the term acts as a sink. In an unstable atmosphere ($N^2 < 0$), air parcels may rise freely, and this term becomes a source. The coefficient K_h is the turbulent heat-exchange coefficient (Stull, 1988; Holton and Hakim, 2013).

- The third term, $c\overline{e}^{3/2}/l_{\text{diss}}$, is the dissipation rate ε, the same quantity measured by the different instruments as summarised in Table B1. It represents the loss of TKE as energy cascades from large eddies to progressively smaller scales and is finally dissipated as heat by molecular viscosity (Kolmogorov, 1962; Stull, 1988). Here l_{diss} is the dissipation length scale (Hinze, 1975) and c is an empirical constant. This term is always a sink.

- The fourth term is vertical diffusion, which describes how turbulent motions transport TKE vertically through the atmosphere. It neither creates nor destroys TKE, but redistributes it between neighbouring layers. Together, the four terms describe the full cycle of turbulence at any point in the atmosphere: how it is generated by shear and convection, suppressed by stable stratification, dissipated into heat, and spread vertically through the column.

The ratio of the buoyancy term $K_h N^2$ to the shear production term $K_m S_V^2$ equals Ri when $K_m = K_h$, as defined in Sect. 3.1. Ri is therefore not a separate concept but a special case embedded within the TKE framework, capturing only the balance between two of the four terms under the assumption that momentum and heat are mixed equally efficiently. Solving the full budget equation without that assumption gives a far more complete picture of the atmosphere's turbulent state.

3.2.1 Numerical Solution

Solving Eq. 4 in practice is not straightforward: the equation is prognostic and nonlinear, and it must be discretised in time. In operational numerical weather prediction, this is done within ICON's physics suite (Doms et al., 2021). We reproduce the same

https://doi.org/10.5194/egusphere-2026-6332
Preprint. Discussion started: 4 November 2026
© Author(s) 2026. CC BY 4.0 License.

numerical scheme here, as implemented in the model, so that TKE can later be derived from observed wind and temperature. Therefore, the prognostic TKE equation is solved for a velocity scale q, defined by:

$$\overline{e} = \frac{1}{2} q^2 \tag{5}$$

Substituting Eq. 5 into Eq. 4, with $\partial\overline{e}/\partial t = q\,\partial q/\partial t$ and $\partial\overline{e}/\partial z = q\,\partial q/\partial z$, gives:

$$q\frac{\partial q}{\partial t} = K_m S_V^2 - K_h N^2 - \frac{c\,q^3}{2^{3/2}\,l_{\text{diss}}} + \frac{\partial}{\partial z}\left(K_e\,q\frac{\partial q}{\partial z}\right) \tag{6}$$

where the last term is the vertical diffusion of TKE. The exchange coefficients for momentum and heat are proportional to the velocity scale, $K_m = l_m q$ and $K_h = l_h q$, with the stability lengths $l_m = S_m\,l$ and $l_h = S_h\,l$, where S_m and S_h are the stability functions of the closure (Doms et al., 2021). The turbulent mixing length l follows Blackadar (1962), $l = \kappa z/(1+\kappa z/\lambda)$, where z is the height above the surface, $\kappa = 0.4$ is the von Kármán constant and $\lambda = \kappa\,l_\infty \approx 200$ m is its asymptotic upper bound, with $l_\infty = 500$ m; in the 30–60 km range, $z \gg l_\infty$, so $l \approx 200$ m. The dissipation length scale is $l_{\text{diss}} = cl$, and c is the dissipation constant of the closure (Doms et al., 2021).

Dividing Eq. 6 by q, which replaces K_m and K_h by the stability lengths l_m and l_h, and discretising over a time step Δt gives:

$$\frac{q^{n+1}-q^n}{\Delta t} = l_m S_V^2 - l_h N^2 - \frac{c\,(q^{n+1})^2}{2^{3/2}\,l_{\text{diss}}} + T_q \tag{7}$$

where the superscripts n and $n+1$ refer to the current and next time steps, and T_q (in $\mathrm{m\,s^{-2}}$) is the tendency of q due to vertical diffusion. Unlike local terms (shear production, buoyancy and dissipation), which act locally at each level, vertical diffusion couples neighbouring atmospheric levels and cannot be integrated point-by-point. Following Raschendorfer (2001), the algorithm is evaluated for a single 1D vertical column and neglects horizontal advection. Vertical diffusion is therefore treated separately from the local terms and its tendency is written as:

$$T_q = \frac{\sqrt{2\,e^d} - q^n}{\Delta t}, \tag{8}$$

where e^d is the diffused TKE profile, obtained at the end of the time step by solving the implicit vertical diffusion equation (see Appendix A). This split treatment of diffusion introduces an error of $\mathcal{O}(\Delta t)$, but it acts on a term that contributes less than 1 % to the TKE budget, so its effect on the calculated TKE is negligible.

Among the local terms, the dissipation term requires particular care because it is nonlinear in q. Treated explicitly, it can destabilise the solution and drive q to unphysical negative values. The model therefore evaluates it at the new time step, as $c(q^{n+1})^2/(2^{3/2}l_{\text{diss}})$, while the shear, buoyancy and diffusion terms use known values (Doms et al., 2021). The stability lengths are taken from the current step, $l_m = K_m^n/q^n$ and $l_h = K_h^n/q^n$, and the shear and buoyancy terms are combined into a single forcing,

$$F = \max\left(l_m S_V^2 - l_h N^2,\; r\,l_m S_V^2\right), \tag{9}$$

https://doi.org/10.5194/egusphere-2026-6332
Preprint. Discussion started: 4 November 2026
© Author(s) 2026. CC BY 4.0 License.

where $r \approx 0.81$ limits how far buoyancy can reduce the shear forcing. Rearranging gives:

$$\frac{c\,\Delta t}{2^{3/2}\,l_{\text{diss}}}\,(q^{n+1})^2 + q^{n+1} = q^n + \Delta t\,(F + T_q) \tag{10}$$

The dissipation term is now grouped implicitly on the left, leaving only known quantities on the right. This removes the need for an iterative solver and keeps q positive. Equation 10 is quadratic in q^{n+1} and can be solved analytically. In the form $A(q^{n+1})^2 + B\,q^{n+1} - C = 0$, with

$$A = \frac{c\,\Delta t}{2^{3/2}\,l_{\text{diss}}}, \qquad B = 1, \qquad C = q^n + \Delta t\,(F + T_q)\,, \tag{11}$$

where the positive real root is:

$$q_{\text{solver}} = \frac{-B + \sqrt{B^2 + 4AC}}{2A} \tag{12}$$

and substituting the definitions of the coefficients gives the solver equation used inside the model:

$$q_{\text{solver}} = \frac{2^{3/2}\,l_{\text{diss}}}{2\,c\,\Delta t}\left[\sqrt{1 + \frac{4\,c\,\Delta t\,[q^n + \Delta t\,(F + T_q)]}{2^{3/2}\,l_{\text{diss}}}} - 1\right] \tag{13}$$

The intermediate value q_{solver} represents the prognostic velocity scale prior to physical limiting and numerical smoothing. To determine the final updated velocity scale q^{n+1}, three conditions are evaluated (Doms et al., 2021). Each corresponds to a different regime, and the largest of the three is taken.

The first is a floor value q_{floor}, which keeps TKE from dropping to zero under very stable conditions where the solver would otherwise return an unrealistically small value. Some residual background mixing is always present in the atmosphere, and the floor accounts for it.

The second is a local equilibrium value:

$$q_{\text{equilibrium}} = \sqrt{l_{\text{frc}}\,F} \tag{14}$$

Here $l_{\text{frc}} \approx 7.3\,l_{\text{diss}}$ is the forcing length scale of the closure, proportional to l. This value acts as a forcing-dependent lower bound that prevents TKE from lagging behind a sudden increase in forcing, as during wave breaking, where turbulence responds faster than the time step allows.

The third is a history value:

$$q_{\text{history}} = w_1\,q^n + w_2\,q_{\text{solver}}, \qquad w_1 + w_2 = 1 \tag{15}$$

Here, $w_1 = 0.15$ and $w_2 = 0.85$ are numerical smoothing weights that blend the new solution with the previous step to damp abrupt changes between time steps. The three values represent different situations, and the largest is taken as the final velocity scale, ensuring the model never underestimates the turbulence actually present. The final velocity scale is:

$$q^{n+1} = \max\left(q_{\text{floor}},\, q_{\text{equilibrium}},\, q_{\text{history}}\right) \tag{16}$$

https://doi.org/10.5194/egusphere-2026-6332
Preprint. Discussion started: 4 November 2026
© Author(s) 2026. CC BY 4.0 License.

Once q^{n+1} has been determined, it is converted back to TKE (e) using Eq. 5:

$$\overline{e}^{n+1} = \frac{1}{2}(q^{n+1})^2 \tag{17}$$

Throughout, we use the same closure constants and stability functions as in the model (Doms et al., 2021). These values are well established within the scheme, and no tuning or adjustment was applied at any stage. The purpose here is not to develop a new turbulence closure but to reproduce an existing and widely used closure scheme outside the model, so that it can be driven by observations of wind and temperature. Any agreement or disagreement with the model TKE therefore reflects the algorithm itself rather than a choice of parameters. The updated value $\overline{e}^{n+1}$ is passed forward to the next time step, and the integration repeats. One requirement still remains before the algorithm can start: specifying the initial TKE at the very first time step.

3.2.2 Initial Conditions

The procedure described above is prognostic, so it requires a TKE value at the first time step to begin.

Since our goal is to apply this method to lidar observations, where no such value exists, an a priori value must be provided instead. Rather than picking an arbitrary number, we take the first value from the wind and temperature themselves, by assuming the turbulence is in local quasi-equilibrium at the initial time step. This corresponds to the diagnostic Level-2 quasi-equilibrium limit of Mellor and Yamada (1974). If the atmosphere is neither gaining nor losing turbulent energy at the first step, the rate of change term in Eq. 4 vanishes, and shear production is balanced by buoyancy and dissipation alone:

$$K_m S_V^2 - K_h N^2 - \frac{c q^3}{2^{3/2} l_{\text{diss}}} = 0 \tag{18}$$

Writing the exchange coefficients in terms of the velocity scale, $K_m = l_m q$ and $K_h = l_h q$, one factor of q cancels from both sides:

$$q_{\text{qe}} = \sqrt{\frac{2^{3/2} l_{\text{diss}}}{c} (l_m S_V^2 - l_h N^2)} \tag{19}$$

Solving for q mathematically yields two roots, and we select the positive root because the velocity scale must be non-negative. Where buoyancy exceeds shear production ($l_m S_V^2 - l_h N^2 \leq 0$), the term inside the square root becomes negative, and no real solution exists; in this case, q_{qe} is set to the background floor value q_{floor}. Because the stability functions determining l_m and l_h depend on q, Eq. 19 is solved iteratively until q_{qe} converges, and the initial TKE is evaluated as $\overline{e}^0 = \frac{1}{2}(q_{\text{qe}})^2$. The effect of this choice is examined in Sect. 4.4.

Taking UA-ICON as a virtual lidar, unlike a real instrument, it is free of measurement noise, and we know exactly what input goes into the algorithm. This allows the method to be tested and developed systematically before it is applied to real observations, where noise and other instrumental effects are unavoidable. We therefore first reproduce the full procedure outside the model, using wind and temperature fields from UA-ICON, and compare the resulting TKE against the model TKE to validate the methodology. The model TKE serves only as a reference for this comparison and is never used as an input: the calculation is driven entirely by wind and temperature, including the initial value. Once validated, the same procedure is applied to real lidar observations.

https://doi.org/10.5194/egusphere-2026-6332
Preprint. Discussion started: 4 November 2026
© Author(s) 2026. CC BY 4.0 License.

3.3 Noise Sensitivity Testing

When working with real observations, there is an important point to consider: instrument data, such as u, v, and temperature, always come with some level of noise. The TKE calculation doesn't depend directly on the wind and temperature, but on their vertical gradients, S_V^2 and N^2. Taking a derivative amplifies noise, so even a modest uncertainty in the measured profile can produce a much larger uncertainty in the shear and the stratification, and therefore in the calculated TKE.

Real lidar observations always contain some level of noise, quantified by the signal-to-noise ratio (SNR). This noise level varies with instrument, altitude, and atmospheric conditions, and achieving sufficient SNR is a recognised concern for lidar wind and temperature data (Yang and Liu, 2022). UA-ICON, however, provides noise-free fields; synthetic noise must be added deliberately to test how the algorithm performs under this kind of realistic, lidar-like uncertainty.

At each height, the noise amplitude is set to a fixed percentage of that variable's range of variation over the full time series. Uniformly distributed random noise, scaled to this amplitude, is then added independently to the wind and temperature fields at every point. Different noise levels are tested, expressed as a signal-to-noise ratio in decibels,

$$\mathrm{SNR}_{\mathrm{dB}} = 20\log_{10}\left(\frac{100}{\text{noise level }[\%]}\right), \tag{20}$$

so that a smaller noise percentage corresponds to a higher SNR. The impact of noise with different amplitudes is presented in Sec. 4.5. As expected, higher-amplitude noise increases the uncertainty of the results. Smoothing is a very common method for suppressing noise in observational data. In Sect. 4.5, we also demonstrate its effect. We deliberately avoid smoothing the data too heavily, since excessive smoothing would remove real structure from the profile along with the noise. For clarity, we perform the smoothing in only one direction (temporal or vertical).

Together, these steps, the TKE budget equation, its numerical solution, the initial condition, and the noise sensitivity test, form the complete methodology applied in the following section, first to UA-ICON and then later to real lidar observations.

4 Results

4.1 Evaluating Ri as a TKE Indicator

Before applying our algorithm, we first investigate whether Ri alone can serve as a reliable indicator of TKE in the atmosphere. As an example, we take model wind and temperature at 54 km and compute Ri using Eq. 1, while the model-derived TKE is extracted from the UA-ICON model.

https://doi.org/10.5194/egusphere-2026-6332
Preprint. Discussion started: 4 November 2026
© Author(s) 2026. CC BY 4.0 License.

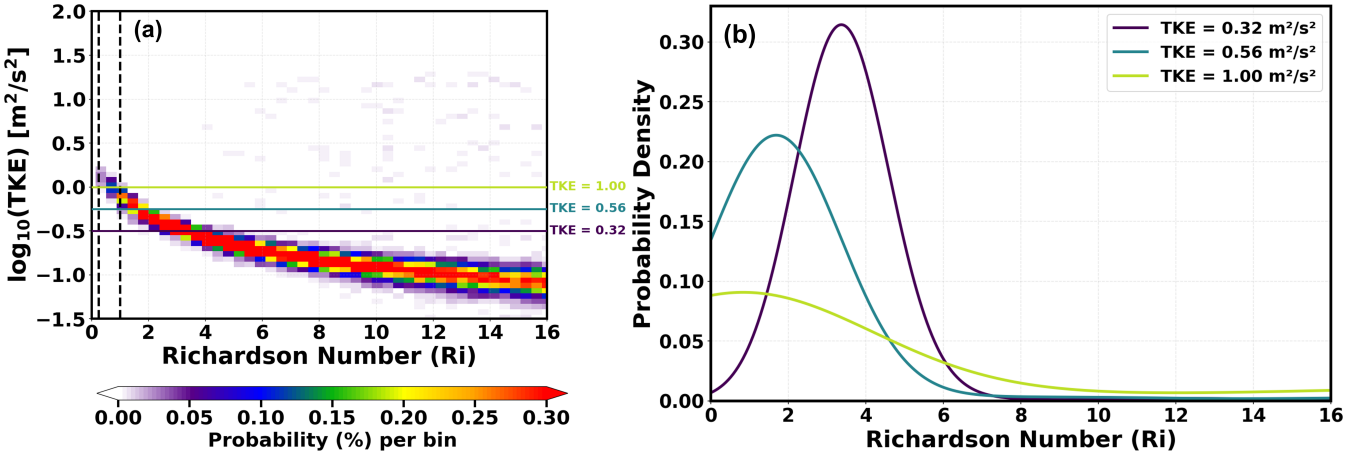


Figure 1. (a) Two-dimensional histogram of $\log_{10}$(TKE) versus Ri at an altitude of 54 km over a 24 h period, computed from UA-ICON model data. The colour indicates the probability (%) per bin. The vertical dashed lines mark Ri = 0.25 and Ri = 1, and the horizontal lines mark fixed TKE values of 0.32, 0.56, and 1.00 m^2/s^2. (b) Probability density of Ri for the same three fixed TKE values at the same altitude.

Figure 1a shows the two-dimensional histogram of $\log_{10}$(TKE) versus Ri at 54 km. The overall downward trend is consistent with the classical criterion: as Ri decreases, TKE tends to increase, reflecting the growing dominance of wind shear over buoyancy. At low Ri values, high TKE is clearly present and well concentrated, which again aligns with the classical instability criterion. However, at lower TKE values, the picture becomes less clear for a fixed TKE; Ri spans a very wide range, making it difficult to infer the turbulence intensity from Ri alone. This is further demonstrated in Fig. 1b, which shows the Ri distributions for three fixed TKE values. In each case, Ri is broadly distributed, ranging from the dynamically unstable region below 0.25 to the stable region well above 1. The three distributions overlap substantially, meaning that the same Ri value can occur across very different turbulence intensities. This investigation clearly suggests that Ri alone is not a sufficient indicator of the actual turbulent energy present in the atmosphere. Turbulence can persist well beyond the classical Ri threshold, and a single Ri value can correspond to very different turbulence intensities, in agreement with Haack et al. (2014) and Grachev et al. (2013).

4.2 TKE Budget Term Contributions

Having shown that Ri alone cannot indicate the magnitude of turbulence, we now examine the relative contribution of each term in the TKE budget equation (Eq. 4), using UA-ICON wind and temperature between 30 and 60 km at fixed latitude and longitude. Figure 2 shows the distribution of shear production, buoyancy, dissipation, and vertical diffusion.

https://doi.org/10.5194/egusphere-2026-6332
Preprint. Discussion started: 4 November 2026
© Author(s) 2026. CC BY 4.0 License.

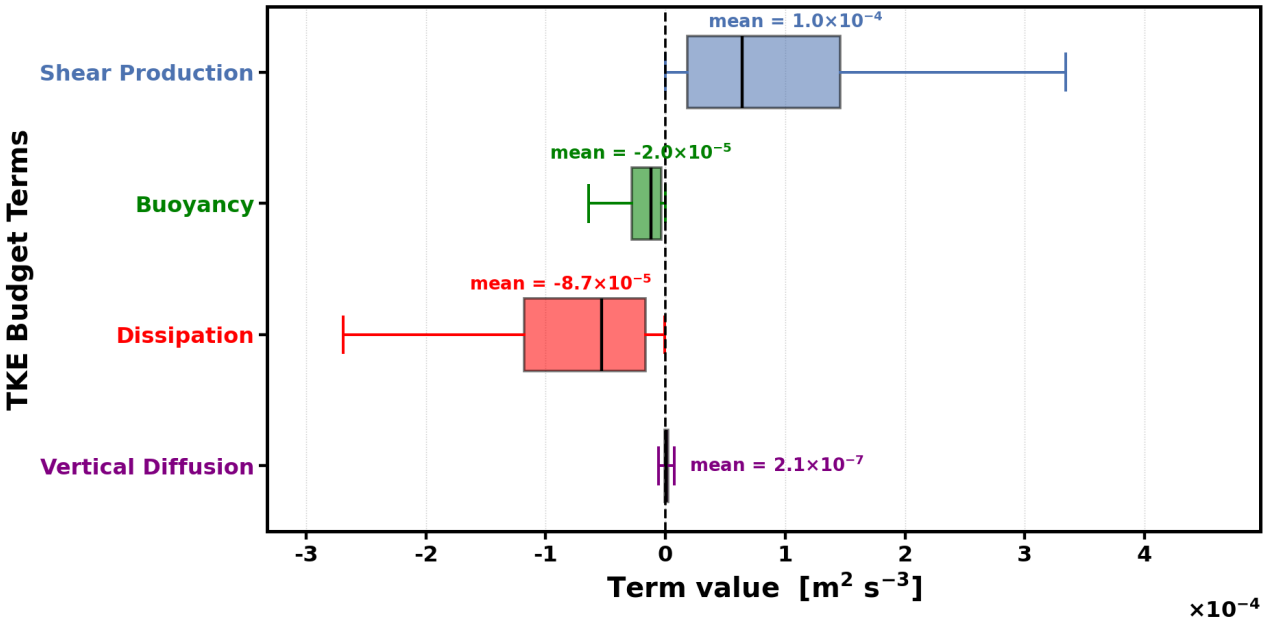


Figure 2. Distribution of the different TKE budget terms (shear production, buoyancy, dissipation, and vertical diffusion) [m^2 s^{-3}] over the altitude range 30 to 60 km, at fixed latitude and longitude over a 24 h period, computed from UA-ICON model data. Boxes show the interquartile range, whiskers show the full range, and the black line inside each box marks the median. Annotated values provide the mean value for each term. The vertical dashed line at zero separates source terms (positive) from sink terms (negative).

Shear production is the dominant source of TKE, exhibiting the widest spread of all four terms, with values ranging from 0.003×10^{-5} to 81×10^{-5} m^2 s^{-3}. Dissipation is the dominant sink, comparable in absolute magnitude to shear production, with values extending from near zero (-0.09×10^{-5}) down to a minimum of -59×10^{-5} m^2 s^{-3}. Buoyancy acts predominantly as a smaller net sink, with values typically ranging between -15×10^{-5} and near zero (-0.001×10^{-5}) m^2 s^{-3}. This is consistent with generally stable stratification suppressing rather than generating turbulence over this altitude range, though it can occasionally act as a source during localised convective instability. Finally, vertical diffusion is negligible by comparison. On average, it is two orders of magnitude smaller than the primary terms and tightly centred around zero, with a narrow overall range from -5.9×10^{-5} to 3.5×10^{-5} m^2 s^{-3}.

Shear production and dissipation are the two largest terms and are comparable in magnitude, so the turbulent state at any point is primarily a balance between the two terms. Buoyancy, though smaller here, can become a leading term under strong or negative stratification, and vertical diffusion, while negligible on average, redistributes energy between layers where sharp gradients occur. We retain the vertical diffusion term to solve the complete budget equation. In our study, we prioritise a physically accurate representation of TKE over computational efficiency.

https://doi.org/10.5194/egusphere-2026-6332
Preprint. Discussion started: 4 November 2026
© Author(s) 2026. CC BY 4.0 License.



4.3 TKE Algorithm Validation

Having established how each term contributes to the TKE budget, we first verified that each individual budget term reproduces the corresponding UA-ICON diagnostic from 30 to 60 km. We find good agreement across all terms: shear production ($r = 0.98$), buoyancy ($r = 1.000$), dissipation ($r = 0.997$), and vertical diffusion ($r = 0.995$). This component-level validation ensures the soundness of our approach before combining them into a full TKE estimate. We now apply the complete algorithm to estimate TKE directly from UA-ICON wind and temperature fields. To test our algorithm, we applied it to model data rather than observations because the model provides wind and temperature data free of measurement noise, allowing us to evaluate our algorithm before considering the complications added by observational uncertainty. Critically, the model also computes TKE directly from its prognostic scheme, providing a 'ground-truth' reference. If our algorithm can reproduce the model's TKE using only vertical profiles of wind and temperature as input, we can be confident in applying the same method to real lidar observations.

https://doi.org/10.5194/egusphere-2026-6332
Preprint. Discussion started: 4 November 2026
© Author(s) 2026. CC BY 4.0 License.

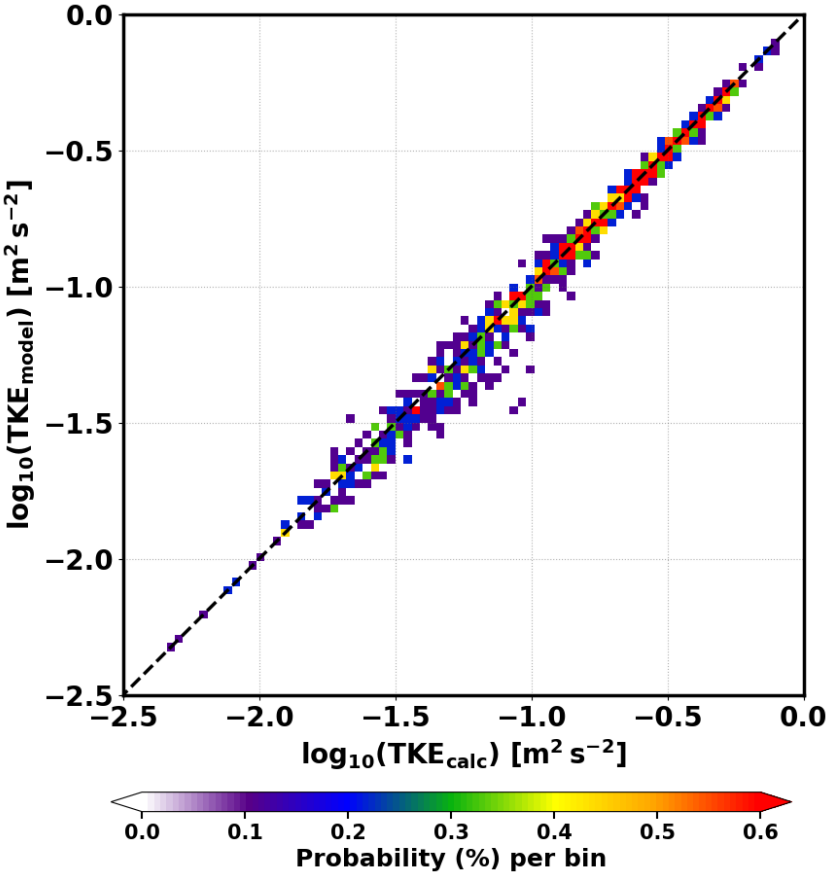


Figure 3. Two-dimensional histogram comparing the calculated TKE from model wind and temperature data (x-axis) with the UA-ICON model TKE output (y-axis) over the altitude range 30 to 60 km, at a fixed latitude and longitude over a 24 h period. Both axes are shown as $\log_{10}$(TKE) [m^2 s^{-2}]. The colour indicates the probability (%) per bin, and the dashed line marks the one-to-one relation. Sample size n = 720.

Figure 3 presents a two-dimensional histogram of calculated TKE versus model TKE across 720 samples in the 30 to 60 km altitude range. The vast majority of points cluster tightly along the one-to-one line, exhibiting a strong positive correlation (r =0.98). This quantitative agreement holds across the full range of TKE values in the dataset, with no systematic bias toward either side of the diagonal. This high degree of correlation demonstrates that our algorithm accurately reconstructs the model's prognostic TKE using only wind and temperature inputs, successfully validating our approach before applying it to observational data.

4.4 Initial Condition Sensitivity

Having validated the full TKE against the model, we now examine the sensitivity of the result to the starting value used in the calculation. The TKE equation we solve is prognostic, meaning we calculate TKE at each time step from the previous

https://doi.org/10.5194/egusphere-2026-6332
Preprint. Discussion started: 4 November 2026
© Author(s) 2026. CC BY 4.0 License.



time step, as described in Sec. 3.2.1. The calculation therefore cannot start on its own; it needs an initial TKE value. When we use the model, this is not a problem because the model TKE is available, so we can simply use it. In the real atmosphere, however, no such value exists. Lidars measure only wind and temperature, and no TKE is observed to start the calculation, so an initial value must be assumed. Initialisation problems are well known and often discussed in lidar technical work (Khanna et al., 2012; Sica and Haefele, 2015) and assuming an a priori value is standard practice. The quasi-equilibrium initialisation introduced in Sect. 3.2.2 provides an a priori starting value for TKE derived from the wind and temperature. This raises an important question: how much of the calculated TKE is actually decided by this assumed starting value rather than by the atmospheric conditions themselves? If the result depends strongly on the initial guess, then the method cannot be applied reliably to observations. We therefore test this directly by repeating the calculation with a wide range of initial TKE values.

https://doi.org/10.5194/egusphere-2026-6332
Preprint. Discussion started: 4 November 2026
© Author(s) 2026. CC BY 4.0 License.

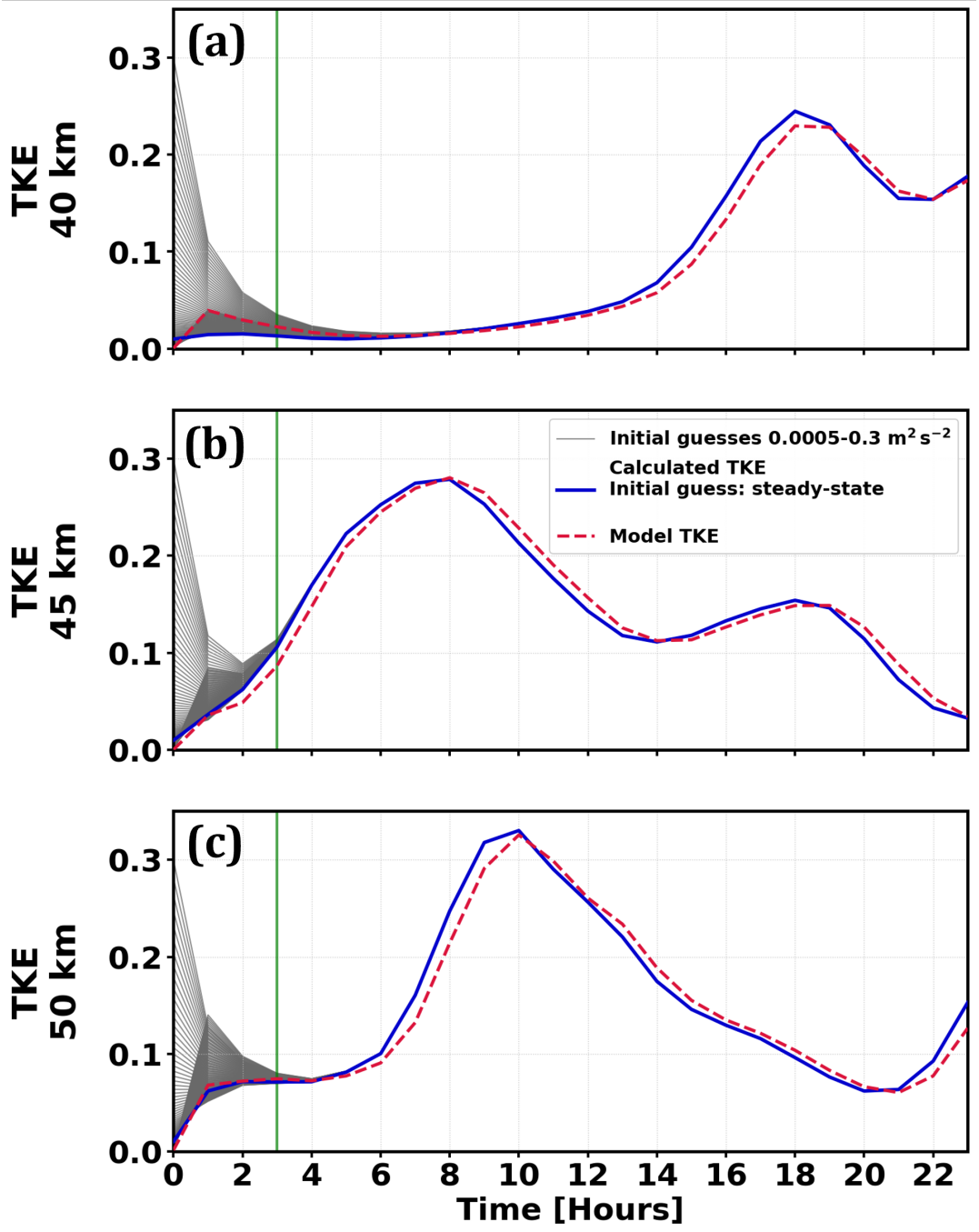


Figure 4. Time evolution of the calculated TKE [$m^2\ s^{-2}$] at a fixed latitude and longitude over 22 h. Panels (a), (b), and (c) show altitudes of 40, 45, and 50 km, respectively. The grey shaded region shows N = 100 separate calculations started from initial TKE values between 0.0005 and 0.3 $m^2\ s^{-2}$. The blue solid line shows the calculation initialised with the quasi-equilibrium solution Eq. 19, and the red dashed line is the TKE from the UA-ICON model at the same altitude. The vertical green line marks approximately where the grey lines converge.

https://doi.org/10.5194/egusphere-2026-6332
Preprint. Discussion started: 4 November 2026
© Author(s) 2026. CC BY 4.0 License.

Figure 4 shows the calculated TKE at three altitudes, 40, 45 and 50 km. The grey lines are separate calculations using the same wind and temperature fields but initialised with different TKE values, ranging from 0.0005 m^2/s^2 (an almost quiescent atmosphere) up to 0.3 m^2/s^2, which is far more turbulent than anything expected at these altitudes. The idea is to start with unrealistic values and see how long that choice matters. At the first time step, the grey lines are spread across the entire range, but this spread converges very quickly. The calculations that overestimate the initial TKE fall rapidly, while those that underestimate it grow similarly. Within about three time steps marked by the green line, they all converge onto a single curve. Beyond this point, the solution can no longer identify the initial value, and all curves follow the model TKE together for the remaining hours. Shear production, buoyancy, and dissipation work together to rapidly pull TKE toward the values the local wind and temperature can sustain, and remove any excess or deficit in the starting value within a few time steps. Atmospheric forcing, not the initial guess, therefore controls the calculated TKE behaviour. The number of time steps, rather than a fixed physical duration, sets this adjustment period. Here the UA-ICON output is hourly, so the roughly three time steps required for convergence correspond to about three hours. Lidar observations are available at a much finer temporal resolution, so the same three time steps would then correspond to only about 15 to 30 minutes. In practice, this means you can discard the first few time steps when applying the method to observations, which costs only a small fraction of a typical measurement and leaves the rest of the time series unaffected by the choice of initial TKE.

However, the initial value need not be arbitrary. As described in Sect. 3.2.2, it can be obtained from the wind and temperature measurements themselves by assuming a quasi-equilibrium solution (Eq. 19), so that the starting value is determined only by the shear and stratification actually present at the first time step rather than by a random guess. Figure 4 shows the resulting time series in blue. The blue line starts close to the model TKE and stays with it from the beginning, without the sharp adjustment seen in the grey curves. The calculated and model TKE agree well for the rest of the time series at all three altitudes. The calculated TKE reproduces the timing and amplitude of the main features, including the strong increase towards 0.25 m^2/s^2 at 40 km late in the day, the broad maximum near 08:00 at 45 km, and the sharp peak close to 0.33 m^2/s^2 at 50 km. The differences that remain are small. The calculated TKE rises slightly earlier than the model at 45 and 50 km, and at 40 km it stays lower than the model during the first few hours, where the model shows a small peak that our calculation does not reproduce. These differences are minor compared with the overall variation of TKE throughout the day.

4.5 Noise Sensitivity

So far, the validation has used clean model fields. However, one further problem remains before applying the method to observations: real lidar profiles always carry measurement uncertainty. We cannot study this uncertainty in the observations themselves because, in a real observation profile, the signal, noise, and wave contributions are already mixed and difficult to separate. By contrast, the model provides noise-free fields with known true TKE, so we can add synthetic noise deliberately, control its level exactly, and quantify its impact against a known reference. This is why we run the noise study on UA-ICON rather than observations. Since the calculation depends on the vertical gradients S_V^2 and N^2 rather than wind and temperature directly, and because taking a derivative amplifies noise, even modest uncertainty in the measured profile can produce much larger uncertainty in the shear and stratification, and therefore in the calculated TKE. We therefore test the

https://doi.org/10.5194/egusphere-2026-6332
Preprint. Discussion started: 4 November 2026
© Author(s) 2026. CC BY 4.0 License.

algorithm's robustness before applying it to observations. As described in Sect. 3.3, we add synthetic noise to the UA-ICON wind and temperature fields at a range of levels, expressed as an SNR in decibels, and repeat the TKE calculation under three smoothing settings: no smoothing, height-dominant smoothing (1 h, 3 km) (green), and time-dominant smoothing (3 h, 1 km) (magenta).

We apply smoothing over a fixed height and time window, but its effect depends on how many data points that window spans, which the input resolution sets. The UA-ICON fields used here have a temporal resolution of one hour and a vertical resolution of roughly 700 m to 1.7 km, so a given smoothing window corresponds to only a few points; on finely resolved lidar profiles the same window would average many more. The window should therefore always be understood relative to the resolution of the data it is applied to.

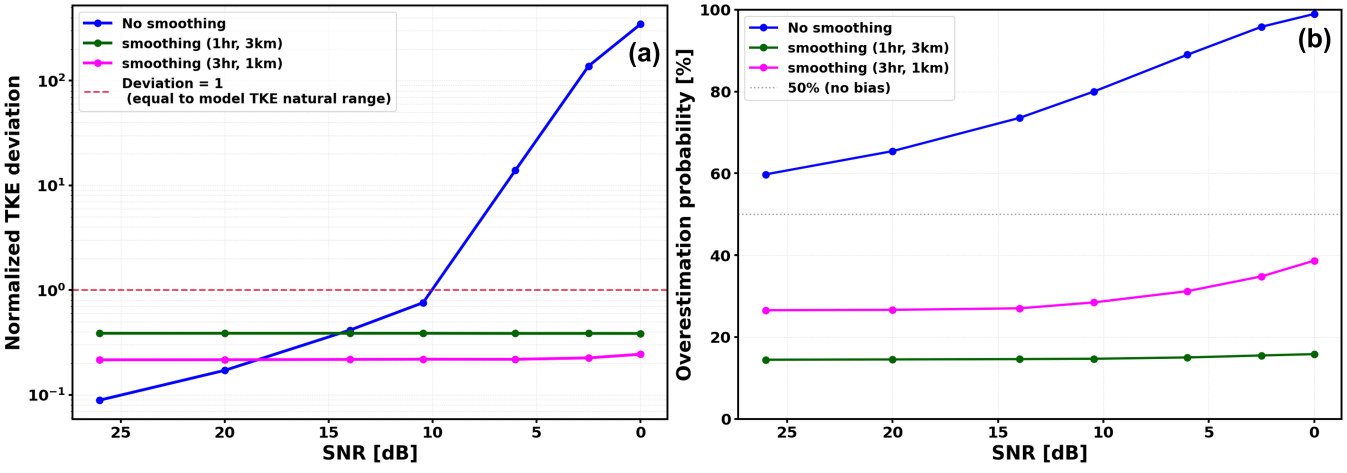


Figure 5. (a) Normalised TKE deviation versus signal-to-noise ratio (SNR) for three smoothing settings applied to UA-ICON model data at a fixed latitude and longitude over a 24 h period: no smoothing (blue), smoothing dominant in height with a 3 km (vertical) by 1 h (temporal) window (green), and smoothing dominant in time with a 1 km (vertical) by 3 h (temporal) window (magenta). The red dashed line marks the threshold where deviation equals the natural range of model TKE. (b) Overestimation probability (%) versus SNR for the same three settings; the dashed line marks 50 % (no bias). In both panels, SNR decreases to the right, so noise increases from left to right.

Figure 5a shows the normalised TKE deviation as a function of SNR, that is, how far the calculated TKE drifts from the model TKE as noise grows. Without smoothing (blue), the deviation is small at high SNR but grows rapidly as noise increases, crossing the model TKE range (red dashed line) near 10 dB and exceeding it by more than an order of magnitude at the noisiest level. This is exactly the behaviour expected when gradients are taken from a noisy profile: the error in S_V^2 and N^2 compounds and quickly overwhelms the result. Applying smoothing removes this growth almost entirely. Both the height-smoothed (green) and time-smoothed (magenta) curves stay flat and low across the whole SNR range, showing that smoothing suppresses the noise-driven amplification before it can build up in the gradients. But a small deviation alone doesn't tell us whether the calculation is too high or too low, which Fig. 5b addresses. We plot how often the calculated TKE overestimates the model value; 50 % (dotted line) means no bias. Without smoothing (blue), the algorithm overestimates in about 60 % of cases at high

https://doi.org/10.5194/egusphere-2026-6332
Preprint. Discussion started: 4 November 2026
© Author(s) 2026. CC BY 4.0 License.

SNR, rising to nearly 90 % as noise increases, so noise not only enlarges the deviation but drives the result systematically too high. Once smoothing is applied, this positive bias disappears, and both settings fall well below the 50 % line, meaning that smoothing consistently pushes the calculated TKE below the true value. This is an unavoidable consequence of smoothing: averaging flattens the sharp shear and stratification features that generate turbulence, so some real TKE is always lost.

The two smoothing settings underestimate by different amounts, and the difference is physically meaningful. Temporal smoothing (magenta) stays closer to the unbiased line (50%), while spatial smoothing in altitude (green) underestimates more strongly, sitting near 15 % across the full range. Vertical smoothing underestimates TKE the most, as expected because the TKE calculation depends on the vertical gradients S_V^2 and N^2, and smoothing in height acts directly on those gradients, whereas time smoothing only has an indirect effect. It therefore reflects how the algorithm will behave on real vertically resolved profiles. The consistent underestimation from vertical smoothing sets a realistic lower bound on the TKE that noisy observations can recover, and this bias must be kept in mind when applying the method to real lidar data.

These results lead to a general recommendation rather than a single fixed conclusion: because noise-driven error and smoothing-driven underestimation trade off against one another, the appropriate amount of smoothing depends on the SNR of the particular dataset. Low-noise profiles need little smoothing and retain more real structure, while noisier profiles require heavier smoothing at the cost of greater low bias. For the lidar analysis that follows (Sect. 5), we apply smoothing of 1.5 km in height and 1.5 h in time. After this smoothing, the SNR of the lidar winds and temperature at 35-60 km, estimated as the ratio of the daily range of each variable to its statistical measurement uncertainty, exceeds 30 dB, well above the usability threshold of about 9.4 dB identified above (Fig. 5). The smoothing thus suppresses gradient noise in these profiles while keeping the underestimation modest, and the resulting TKE should be regarded as a lower estimate of the actual turbulence.

5 Application to Lidar Observations

Having validated the algorithm against UA-ICON and characterised its response to simulated noise, we now apply it to real lidar observations. We apply the same algorithm, with the same closure constants and stability functions, to wind and temperature measurements from the ALOMAR RMR lidar. Two adjustments follow from the preceding sections. The profiles are gridded at a resolution of 150 m by 5 minutes, and are first smoothed using a 2D Gaussian filter with a full width at half maximum of 1.5 km in altitude and 1.5 h in time, which, as shown in Sect. 4.5, suppresses the noise-driven amplification of the gradients S_V^2 and N^2 before it accumulates in the calculated TKE. We then discard the first few time steps, since the initial-condition test (Sect. 4.4) showed that the influence of the assumed starting value disappears within about three time steps, corresponding to roughly 15–30 min at lidar resolution.

https://doi.org/10.5194/egusphere-2026-6332
Preprint. Discussion started: 4 November 2026
© Author(s) 2026. CC BY 4.0 License.

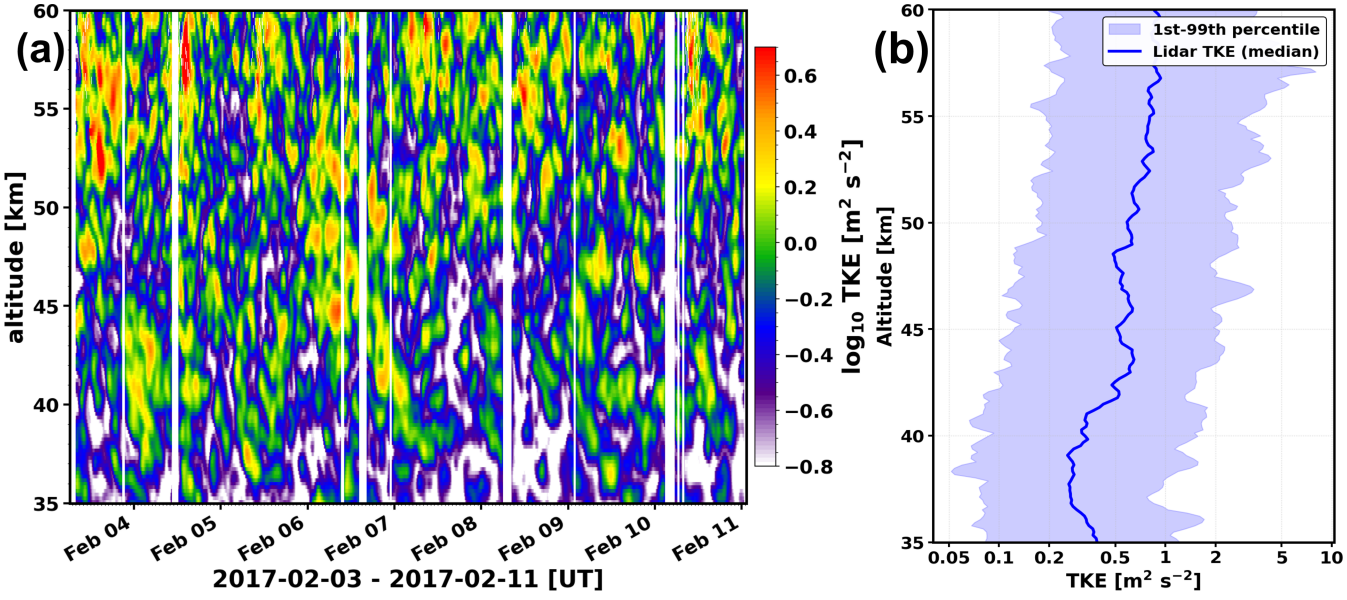


Figure 6. TKE calculated from ALOMAR RMR lidar wind and temperature measurements (69.28°N, 16.01°E) between 35 and 60 km altitude for 3–11 February 2017 (187 h). **(a)** Time–height section of TKE, shown as $\log_{10}$ of TKE in $\mathrm{m^2\ s^{-2}}$. White stripes mark observation gaps. **(b)** Median TKE profile in $\mathrm{m^2\ s^{-2}}$ over the full period (blue line) and the range between the minimum and maximum (1st–99th percentile) at each altitude (shading).

Figure 6 provides, for the first time, a quantitative estimate of turbulent kinetic energy in the middle atmosphere derived solely from lidar wind and temperature measurements at 69.28°N, 16.01°E. As summarised in Table B1, no turbulence measurements exist in the 35–60 km altitude range; in-situ rockets, balloons, and ground-based radars operate outside this region, leaving it largely unexplored. As a result, we have no other observations to compare our results against. These results show that a full prognostic TKE budget, driven exclusively by observed wind and temperature, allows us to access this previously unmeasured altitude range. The calculated TKE reveals turbulence as intermittent, highly structured patches rather than continuous layers, with a minimum of $0.09\ \mathrm{m^2\ s^{-2}}$ and a maximum of $2.8\ \mathrm{m^2\ s^{-2}}$ (1st–99th percentile) and a median of $0.54\ \mathrm{m^2\ s^{-2}}$. Figure 6b shows the median TKE profile over the full period together with the 1st–99th percentile range at each altitude, with TKE increasing with altitude. Rather than providing a single snapshot, the algorithm recovers turbulence continuously over nearly eight days at a few-minute temporal resolution, capturing variability in both altitude and time. The vertical white stripes in Fig. 6 indicate interruptions in the lidar record due to cloud cover, which blocks the upward laser beam. These results provide proof of concept that the method works on real observations and enable the calculation of TKE using long-term lidar wind and temperature measurements, as described in Sect. 1.3. Future work will include a more detailed analysis of additional lidar profiles, including direct comparisons with model TKE.

https://doi.org/10.5194/egusphere-2026-6332
Preprint. Discussion started: 4 November 2026
© Author(s) 2026. CC BY 4.0 License.

6 Discussion

No direct measurements of TKE or dissipation rate exist between 35 and 60 km (Table B1). The observational studies listed there reach about 35 km with balloon-borne instruments and resume above 60 km with sounding rockets. Most of them report the dissipation rate ε rather than TKE; the few that measure TKE directly do so from towers and research aircraft, and none reach beyond about 14 km. Reference values for our altitude range therefore come from atmospheric models, and the TKE they report from the surface up to 100 km is summarised in Table B2.

The numerical modelling studies compiled in Table B2 span several distinct vertical domains and dynamical settings. Since TKE increases with altitude, the reported values differ between altitude ranges. Several studies focus strictly on convective and stable boundary layers below 3 km (Nakanishi and Niino, 2009; He et al., 2019; Kumar et al., 2021; Tkachenko et al., 2020; MacDonald and Teixeira, 2020; Bašták Ďurán et al., 2022), reporting TKE values ranging from a stable background floor of $\sim 10^{-3}\,\mathrm{m^2\,s^{-2}}$ up to active daytime convective peaks reaching $2.8\,\mathrm{m^2\,s^{-2}}$. Other studies investigate mountain-wave breaking extending into the upper troposphere and lower stratosphere (UTLS, up to 14–15 km) (Elvidge et al., 2017; Siri Jagan and Schmidli, 2026), with modelled TKE values generally between 0.01 and $5.0\,\mathrm{m^2\,s^{-2}}$ (and localised severe breaking reaching up to $30\,\mathrm{m^2\,s^{-2}}$). For whole-atmosphere models spanning the full column from the surface up to 100–135 km—which directly encompass our 35–60 km observation range—simulations by Avsarkisov et al. (2022) and Banerjee et al. (2026) report TKE values ranging from 10^{-3} to $6.1\,\mathrm{m^2\,s^{-2}}$. Finally, over the same 30–60 km altitude range, the 1.25 km UA-ICON nest over ALOMAR analysed by Morfa et al. (2026) has a mean turbulent kinetic energy of $0.48\,\mathrm{m^2\,s^{-2}}$, with a standard deviation of $1.81\,\mathrm{m^2\,s^{-2}}$ across the sampled locations, heights and times on 23 March 2023.

Our ALOMAR lidar retrievals (35–60 km) yield TKE values between 0.09 and $2.8\,\mathrm{m^2\,s^{-2}}$ (1st to 99th percentile) with a median of $0.54\,\mathrm{m^2\,s^{-2}}$. Because the algorithm applies the ICON closure unchanged, these values represent the TKE that the ICON scheme would diagnose from the observed atmosphere, and future comparisons with co-located model runs would therefore test the model rather than the metric. Comparing this range against the literature shows that our middle-atmospheric values fall well within the reported model ranges. In particular, our median value of $0.54\,\mathrm{m^2\,s^{-2}}$ is consistent with the typical turbulence levels simulated by Avsarkisov et al. (2022) and Banerjee et al. (2026), which directly cover our altitude range, and closely matches the mean TKE of $0.48\,\mathrm{m^2\,s^{-2}}$ reported by Morfa et al. (2026) over the same 30–60 km range. This consistency confirms that our retrieved TKE values are physically reasonable and quantitatively comparable to existing turbulence modelling studies. However, we emphasise that this serves as a general consistency check rather than a direct, one-to-one validation. With the UA-ICON data used in this study, an exact quantitative match cannot be expected due to substantial differences in spatial and temporal sampling, as well as differing altitude coverage. In addition, the lidar retrieval represents a sample of 187 hours of clear-sky observation windows rather than a continuous long-term climatology. In the future, a more direct comparison would be possible by conducting dedicated high-resolution regional model simulations centred over ALOMAR for specific case-study periods matching concurrent lidar observations, as well as by constructing an extended lidar climatology from a larger profile dataset to investigate seasonal variations.

https://doi.org/10.5194/egusphere-2026-6332
Preprint. Discussion started: 4 November 2026
© Author(s) 2026. CC BY 4.0 License.

7 Summary and Conclusions

In this study, we developed a method to estimate TKE in the middle atmosphere directly from lidar wind and temperature observations by applying the prognostic TKE budget of the ICON physics package outside the model. We first validated the method against UA-ICON and then applied it to observations from the ALOMAR RMR lidar. We began by examining whether Ri alone is sufficient to indicate turbulence intensity. Using wind and temperature from the UA-ICON model, we found that the expected inverse relationship between Ri and TKE is present, but that a single TKE value corresponds to a broad range of Ri, extending from the dynamically unstable region below 0.25 well into the stable region above 1, and that the Ri distributions for different TKE values overlap heavily. Ri therefore indicates where turbulence is likely, but not how much turbulent energy is present, consistent with earlier observational studies (Haack et al., 2014; Grachev et al., 2013).

To obtain quantitative values, we implemented the prognostic TKE equation used in ICON's physics suite (Doms et al., 2021) as an algorithm driven only by wind and temperature, using the same closure constants and stability functions as the model, with no tuning at any stage. Examining the individual budget terms showed that shear production and dissipation are the two dominant and closely balanced terms, while buoyancy acts as a smaller sink and vertical diffusion is negligible on average; this complete budget equation is needed to capture the turbulent state correctly.

Because the equation is prognostic, it requires an initial TKE value that observations do not provide. We showed that this dependence is short-lived: starting values spanning nearly three orders of magnitude, from 0.0005 to 0.3 $m^2\ s^{-2}$, converge onto a single solution within about three time steps, after which the evolution is controlled by the wind and temperature forcing rather than by the initial guess. This dependence can be removed altogether by using the quasi-equilibrium solution of the TKE equation, which fixes the starting value from the shear and stratification present at the first time step. When applied to UA-ICON, the algorithm reproduced the model TKE closely, with most samples clustered along the one-to-one line and no systematic offset, confirming that it reconstructs the model's prognostic TKE from wind and temperature alone, with no TKE input from the model at any stage.

Because lidar profiles carry measurement uncertainty, and the calculation depends on the vertical gradients S^2 and N^2 rather than on the wind and temperature directly, we quantified the effect of noise using synthetic, lidar-like noise added to the model fields. Without smoothing, noise amplifies through the gradients and systematically drives the calculated TKE too high. Smoothing suppresses this amplification effectively, but at the cost of a modest low bias, since averaging also flattens the sharp gradients that generate turbulence; height smoothing, which acts directly on the vertical gradients, underestimates by up to about 15 %. Temporal smoothing has less of an effect on the TKE than vertical smoothing. The appropriate amount of smoothing therefore depends on the dataset's temporal and vertical resolution, and the recovered TKE should be regarded as a lower estimate of the true turbulence.

Finally, we applied the validated algorithm to real wind and temperature observations from the ALOMAR RMR lidar. This is the first time that a full prognostic TKE budget, of the kind used in atmospheric models, has been applied to real observations to obtain a quantitative estimate of TKE in the middle atmosphere, an altitude range (35–60 km) where turbulence has not previously been measured (Table B1). The calculated lidar TKE resolves turbulence as thin, intermittent, and patchy layers,

https://doi.org/10.5194/egusphere-2026-6332
Preprint. Discussion started: 4 November 2026
© Author(s) 2026. CC BY 4.0 License.

demonstrating that the method works on real observations and opening this altitude range to quantitative turbulence estimation for the first time.

This study established and validated the method against UA-ICON and applied it to calculate TKE directly from lidar wind and temperature, showing that observations alone can drive a full prognostic TKE budget. For future studies, the method can be applied to long-term observational records of wind and temperature. This would enable the first TKE climatologies in the middle atmosphere derived from lidar observations and allow us to study how turbulence varies with altitude, season, and atmospheric conditions. Later, more detailed validation may also become possible with higher-resolution model data, where the grid is fine enough to resolve the same sharp shear and stratification features seen in the observations, allowing a fairer, co-located comparison between calculated and model TKE. Turbulence quantified in this way from observations could then serve as a useful reference for testing and improving the turbulence schemes used in general circulation models.

Code availability. All codes used in this paper are available under Goswami (2026b).

Data availability. The data files to reproduce all figures in this study are available from the RADAR repository (Goswami, 2026a). The DOI will be provided by RADAR after acceptance.

Appendix A: Implicit Tridiagonal Discretization of Vertical TKE Diffusion

This appendix presents the discrete tridiagonal matrix formulation and the two-sweep Thomas algorithm for the 1D implicit vertical diffusion of turbulent kinetic energy (TKE) described by Eq. 8.

A1 Governing Kinematic Equation

In Section 3.2, the 1D vertical diffusion of TKE is evaluated in kinematic form:

$$\frac{\partial e}{\partial t} = \frac{\partial}{\partial z}\left(K_e \frac{\partial e}{\partial z}\right), \tag{A1}$$

where $K_e(z) = c_{\text{diff}}\, l(z)\, q(z)$ is the turbulent exchange coefficient with $c_{\text{diff}} = 0.2$, master mixing length $l(z)$, and velocity scale $q = \sqrt{2e}$.

A2 Grid Staggering and Finite-Volume Discretization

The vertical domain is discretized into K layer centers (full levels, indexed $k = 1, \ldots, K$ from top to bottom) and $K+1$ layer interfaces (half levels, indexed $k \pm 1/2$). The prognostic variables e_k, q_k, and the layer thickness $\Delta z_k = z_{k-1/2} - z_{k+1/2}$ are defined at full levels k. The interfacial exchange coefficients $K_{e,k+1/2}$ and the vertical level separation $\Delta z_{k+1/2} = z_k - z_{k+1}$

https://doi.org/10.5194/egusphere-2026-6332
Preprint. Discussion started: 4 November 2026
© Author(s) 2026. CC BY 4.0 License.

are defined at half levels $k+1/2$, with:

$$K_{e,k+1/2} = \frac{1}{2}\left(K_{e,k} + K_{e,k+1}\right). \tag{A2}$$

Integrating Eq. (A1) over layer k from time step t^n to $t^{n+1} = t^n + \Delta t$ under a backward-implicit Euler scheme yields:

$$\frac{\Delta z_k}{\Delta t}\left(e_k^d - e_k^n\right) = \mathcal{F}_{k-1/2}^d - \mathcal{F}_{k+1/2}^d, \tag{A3}$$

where e_k^d is the diffused TKE profile and $\mathcal{F}_{k+1/2}^d$ is the downward diffusive energy flux across interface $k+1/2$:

$$\mathcal{F}_{k+1/2}^d = K_{e,k+1/2}\left(\frac{e_k^d - e_{k+1}^d}{\Delta z_{k+1/2}}\right). \tag{A4}$$

Defining the discrete cell capacity D_k and the interfacial conductance $M_{k+1/2}$ as:

$$D_k \equiv \frac{\Delta z_k}{\Delta t}, \qquad M_{k+1/2} \equiv \frac{K_{e,k+1/2}}{\Delta z_{k+1/2}}, \tag{A5}$$

Eq. (A3) can be written in balance form:

$$D_k\left(e_k^d - e_k^n\right) = M_{k-1/2}\left(e_{k-1}^d - e_k^d\right) - M_{k+1/2}\left(e_k^d - e_{k+1}^d\right). \tag{A6}$$

A3 Tridiagonal Matrix System

Rearranging terms for interior levels $k = 2, \ldots, K-1$ yields the linear tridiagonal system:

$$-a_k\, e_{k-1}^d + b_k\, e_k^d - c_k\, e_{k+1}^d = d_k, \tag{A7}$$

with coefficients:

$$a_k = M_{k-1/2}, \tag{A8}$$

$$c_k = M_{k+1/2}, \tag{A9}$$

$$b_k = D_k + a_k + c_k, \tag{A10}$$

$$d_k = D_k\, e_k^n. \tag{A11}$$

The main diagonal b_k is strictly diagonally dominant since $b_k > a_k + c_k$ for any positive $D_k > 0$, guaranteeing unconditional numerical stability.

For observations sampled on a uniform vertical grid spacing Δz (e.g., $\Delta z = 150$ m), dividing Eq. (A7) by $\Delta z/\Delta t$ simplifies the system to dimensionless interfacial Fourier numbers:

$$\mu_{k+1/2} \equiv \frac{\Delta t}{\Delta z^2} K_{e,k+1/2}, \tag{A12}$$

giving the compact coefficients:

$$a_k = \mu_{k-1/2}, \qquad c_k = \mu_{k+1/2}, \qquad b_k = 1 + a_k + c_k, \qquad d_k = e_k^n. \tag{A13}$$

https://doi.org/10.5194/egusphere-2026-6332
Preprint. Discussion started: 4 November 2026
© Author(s) 2026. CC BY 4.0 License.

A4 Boundary Conditions

At the top of the domain ($k = 1$), a zero-flux Neumann condition is applied across the upper interface ($\mathcal{F}^d_{1/2} = 0$, so $M_{1/2} = 0$ and $a_1 = 0$), yielding:

$$b_1 = D_1 + M_{3/2}, \qquad c_1 = M_{3/2}, \qquad d_1 = D_1\, e^n_1. \tag{A14}$$

On a uniform vertical grid, this simplifies to $b_1 = 1 + \mu_{3/2}$, $c_1 = \mu_{3/2}$, and $d_1 = e^n_1$.

At the bottom of the domain ($k = K$), two boundary treatments are possible:

- *Fixed concentration (ICON operational default):* The bottom value is held unchanged during diffusion ($e^d_K = e^n_K$), corresponding to $a_K = 0$, $b_K = 1$, $c_K = 0$, and $d_K = e^n_K$.
- *Zero-flux Neumann (conservative formulation):* Enforcing $\mathcal{F}^d_{K+1/2} = 0$ gives $M_{K+1/2} = 0$, $c_K = 0$, and $b_K = D_K + M_{K-1/2}$ (or $b_K = 1 + \mu_{K-1/2}$ on a uniform grid), which conserves column-integrated TKE to machine precision.

A5 Solution via the Thomas Algorithm

The tridiagonal linear system (A7) is solved using the standard two-sweep Thomas algorithm:

$$c'_k = \frac{c_k}{b_k - a_k\, c'_{k-1}}, \qquad d'_k = \frac{d_k + a_k\, d'_{k-1}}{b_k - a_k\, c'_{k-1}} \qquad (k = 1, \ldots, K), \tag{A15}$$

$$e^d_k = d'_k + c'_k\, e^d_{k+1} \qquad (k = K, \ldots, 1), \tag{A16}$$

initialized with $c'_0 = d'_0 = 0$ and $e^d_{K+1} = 0$ (recalling $a_1 = c_K = 0$ from boundary zero-flux).

A6 Conversion to Velocity Scale Tendency T_q

Once the diffused profile e^d_k is obtained, the effective velocity scale tendency $T_{q,k}$ is computed following Eq. 8:

$$T_{q,k} = \frac{\sqrt{2\, e^d_k} - q^n_k}{\Delta t}. \tag{A17}$$

This tendency $T_{q,k}$ is then coupled into the prognostic quadratic solver (Eqs. 10–13).

Appendix B: Overview of observational and model turbulence studies

https://doi.org/10.5194/egusphere-2026-6332
Preprint. Discussion started: 4 November 2026
© Author(s) 2026. CC BY 4.0 License.

Table B1. Overview of selected observational studies of atmospheric turbulence using different methodologies reporting the energy dissipation rate ε or turbulent kinetic energy (TKE), at any altitude from the surface layer to the mesosphere.

Author	Dataset used	Altitude range	What they measure	Method used	Quantity derived
Strelnikov et al. (2026)	45 TOTAL/CONE sounding rocket flights, Andøya (69°N) and ESRANGE (68°N), 1990–2025	60–100 km	Neutral air density fluctuations (rocket-borne ionization gauges at sub-metre resolution)	Continuous wavelet transform and Heisenberg theoretical spectral model fitting (100 m resolution climatology)	$\varepsilon \sim 10^{-2}$–500 mW kg^{-1}
Latteck et al. (2005)	3.17 MHz Doppler radar, Andenes, Norway (69°N); Sep 2003–Summer 2004	60–80 km	Doppler backscatter signal spectra from vertical and oblique beams (1 km resolution)	Doppler spectral width method with beam- and shear-broadening correction based on antenna radiation patterns	$\varepsilon \sim$ 5–20 mW kg^{-1}
Theuerkauf et al. (2011)	LITOS balloon, Kühlungsborn (54°N, 12°E) and Kiruna (67°N, 21°E)	0–35 km	Wind fluctuations at ∼cm resolution (constant temperature anemometer)	Spectral fit across the inertial to viscous subrange transition	$\varepsilon \sim$ 10–35 mW kg^{-1}
Clayson and Kantha (2008)	FASTEX (285 2-s soundings, Ireland) and 2005 operational soundings (Tallahassee, Denver; 6-s); troposphere and lower stratosphere	0–30 km	High-resolution radiosonde potential temperature profiles (2-s / ∼10 m and 6-s / ∼30 m resolution)	Thorpe analysis (L_T, $C_K = 0.3$); reordering of potential temperature to infer $\varepsilon = C_K L_T^2 N^3$ and eddy diffusivity K	$\varepsilon \sim 10^{-3}$–10 mW kg^{-1}

https://doi.org/10.5194/egusphere-2026-6332
Preprint. Discussion started: 4 November 2026
© Author(s) 2026. CC BY 4.0 License.

Author	Dataset used	Altitude range	What they measure	Method used	Quantity derived
Satheesan and Krishna Murthy (2002)	Gadanki, India (13.5° N, 79.2° E); tropical troposphere and lower stratosphere (44 nights in winter 1999)	3.75–25 km	VHF MST radar vertical wind time series (45-s sampling, 150 m vertical resolution)	Vertical wind variance method ($\varepsilon = 0.97\overline{w^2}N$) integrating temporal spectra from N to Nyquist; N retrieved from vertical wind spectra	$\varepsilon \sim 0.01$–12 mW kg^{-1}
Nastrom and Eaton (1997)	White Sands Missile Range, New Mexico; 5-year climatology (1991–1995); free troposphere and lower stratosphere	5–20 km	50 MHz VHF radar (15° oblique beam, 150 m range resolution) and El Paso soundings (N)	Doppler spectral width method ($\varepsilon = A^{-3/2}N\sigma^2_{\text{turbc}}$); corrections for beam, shear, and gravity wave broadening; lognormal statistics	$\varepsilon \sim 0.03$–32 mW kg^{-1}
Bramberger et al. (2020)	HALO research aircraft (10 Hz gust probe) and SAFIRE Falcon; mountain-wave encounter above Iceland, October 2016	11.8–13.8 km	In situ 3D wind fluctuations, potential temperature, lidar and cloud radar	Subleg variance decomposition (4–16 km windows) for TKE; inertial dissipation technique for ε	$\varepsilon \sim 0.1$–59 mW kg^{-1}; TKE ~ 0.1–11 m^2 s^{-2}
Sharman et al. (2014)	Over 137 million automated in situ reports from ∼200 commercial aircraft; continental US; UTLS ($\geq$ FL200) and climb/descent profiles	6–13 km	Vertical acceleration and derived vertical winds at 8 Hz (B757 and B737 fleets)	von Kármán spectral model; aircraft response and MLE spectral fitting; PIREP calibration	$\varepsilon \sim 10^{-3}$–370 mW kg^{-1}

https://doi.org/10.5194/egusphere-2026-6332
Preprint. Discussion started: 4 November 2026
© Author(s) 2026. CC BY 4.0 License.

Author	Dataset used	Altitude range	What they measure	Method used	Quantity derived
Cohn (1995)	Millstone Hill, Massachusetts; troposphere (3 case studies during ERICA, Feb 1989)	0–10 km	Millstone Hill 440 MHz UHF radar (1° beam, 300 m pulse) and Hanscom Field CLASS soundings	Comparison of backscatter power method (via C_n^2, sounding M and N, Aeronomy Lab F model) vs Doppler spectral width method corrected for shear/beam broadening	$\varepsilon \sim 10^{-2}$–60 mW kg^{-1}
Nilsson et al. (2016)	BLLAST field campaign (southern France); 10 fair-weather afternoon IOP days	0–1.5 km	Near-surface 3D wind and temperature fluctuations (20 Hz CSAT), UHF profiler	Eddy covariance and inertial subrange spectral fitting; full hourly surface TKE budget	$\varepsilon \sim 1.5$–6.1 mW kg^{-1}; TKE ~ 0.37–1.35 m^2 s^{-2}
Xian et al. (2025)	Shiyan Base, Shenzhen, China; atmospheric boundary layer (2022, 279 clear days)	0.03–1 km	Coherent Doppler wind lidar (0.2 Hz, 30 m) and 356 m tower 3D ultrasonic anemometers	Inertial subrange spectral fitting and full TKE budget analysis	$\varepsilon \sim 10^{-3}$–5 mW kg^{-1}

https://doi.org/10.5194/egusphere-2026-6332
Preprint. Discussion started: 4 November 2026
© Author(s) 2026. CC BY 4.0 License.

Table B2. Overview of modelling studies that compute turbulent kinetic energy (TKE), from the surface layer to the mesosphere and lower thermosphere.

Author	Model and case	Altitude range	What they simulate	Method used	TKE
Avsarkisov et al. (2022)	KMCM (GW-resolving GCM, T240L190); validated against Andenes MF radar	0–135 km	Mesoscale kinetic energy (E_k) and small-scale Kolmogorov RMS velocity ($U_o = \sqrt{\varepsilon/N}$)	Smagorinsky-type Richardson-dependent diffusion; stratified vs. Kolmogorov scaling	$\sim 10^{-3}$–$0.8\,\mathrm{m^2\,s^{-2}}$
Banerjee et al. (2026)	UA-ICON (R2B04, L120, top 150 km) coupled with MS-GWaM; 8-year January ensemble	0–100 km	Prognostic TKE, GW-induced shear (S_{gw}), wave drag, and tracer mixing	Bidirectional coupling of 3D transient GW parameterisation with prognostic 1D TKE scheme	$\sim 10^{-3}$–$6.1\,\mathrm{m^2\,s^{-2}}$
Morfa et al. (2026)	UA-ICON (UA-ICON-2.1, 180 levels, top 150 km); 4 one-way nests over ALOMAR; DOM5 (1.25 km), 300 km × 300 km area; VortEx campaign (23 March 2023)	30–60 km	Prognostic TKE on native model half levels; Blackadar mixing length ($l_\infty = 500$ m, $l \to 200$ m)	Prognostic level-2.5 closure (Raschendorfer, 2001); reference $Ri_c \approx 0.94$, with production possible above this value	0.021–$6.58\,\mathrm{m^2\,s^{-2}}$ (1st–99th percentiles)
Siri Jagan and Schmidli (2026)	ICON-NWP ($\Delta x = 0.5$–2 km, $\Delta z \leq 200$ m in UTLS); DEEPWAVE mountain-wave case (New Zealand)	0–15 km	Model 3D wind, vertical velocity, gravity-wave momentum flux (τ), and prognostic TKE	Operational prognostic TKE scheme (Raschendorfer, 2001) vs. 2TE scheme and nested 130 m LES	~ 0.01–$5.0\,\mathrm{m^2\,s^{-2}}$
Elvidge et al. (2017)	MetUM (N768, ∼17 km horizontal, 70 levels, $\Delta z \approx 400$ m at cruise level); 17-month GADS aircraft verification (UTLS cruise level, Greenland 58°–72°N)	8–14 km	Resolved vertical wind shear, stability (N^2), and diagnosed wave-resolved TKE	First-order mixing-length closure driven by resolved mountain waves with long-tail $f(Ri)$	~ 0.04–$30\,\mathrm{m^2\,s^{-2}}$

https://doi.org/10.5194/egusphere-2026-6332
Preprint. Discussion started: 4 November 2026
© Author(s) 2026. CC BY 4.0 License.

Author	Model and case	Altitude range	What they simulate	Method used	TKE
Bašták Ďurán et al. (2022)	ICON SCM/CRM ($\Delta x = 5$ km, 90 levels) and LAM ($\Delta x \approx 2$ km); GABLS1, BOMEX, DYCOMS-II, ARM, and FESSTVaL cases	0–3 km	Modelled prognostic TKE (e_k), total turbulence energy (e_s), cloud fraction, and turbulent fluxes	Two-energy (2TE) closure coupled to an assumed PDF (APDF) method with blended flux Richardson number Ri_f^*	~ 0.01–$2.8\,\mathrm{m^2\,s^{-2}}$
Nakanishi and Niino (2009)	MYNN Levels 2.5/3 closure (50 levels, $\Delta z = 40$ m, $\Delta t = 2$ s); Wangara Day 33 convective boundary layer	0–2.0 km	Prognostic TKE ($q^2/2$), turbulent master length scale (L), and heat/moisture fluxes	Improved Mellor–Yamada closure with buoyancy-dependent pressure covariances and stability-dependent L	~ 0.05–$2.3\,\mathrm{m^2\,s^{-2}}$
Kumar et al. (2021)	WRF-LES ($\Delta x = 12$ m, 88 levels, $\Delta t = 0.01$ s); convective boundary layer (SWiFT site, Texas; top ∼600 m)	0–1.6 km	Resolved 3D wind, temperature fluctuations, and resolved TKE budget terms	Large-eddy simulation with stochastic cell momentum perturbation (SCPM-M)	~ 0.01–$1.6\,\mathrm{m^2\,s^{-2}}$
He et al. (2019)	CanAM4 SCM (53 levels, 11 levels in lowest 800 m; $\Delta t = 5$ min); Cabauw and DYCOMS-II cases	0–1.5 km	Model wind, potential temperature, moisture, and TKE budget terms	Quasi-equilibrium TKE closure ($\partial k/\partial t \approx 0$) with non-local transport and stability-dependent $Pr(Ri)$	~ 0.01–$0.75\,\mathrm{m^2\,s^{-2}}$
Tkachenko et al. (2020)	Single-column k–ε model (256 levels, $\Delta z = 9$ m, domain 0–2.3 km); convective boundary layer and evening transition (top ∼800 m)	0–1.0 km	Modelled wind, potential temperature, TKE (E_k), and dissipation rate (ε)	Standard two-equation k–ε closure; analysis of TKE power-law decay ($E_k \propto t^{-\alpha}$)	$\sim 10^{-3}$–$1.5\,\mathrm{m^2\,s^{-2}}$

https://doi.org/10.5194/egusphere-2026-6332
Preprint. Discussion started: 4 November 2026
© Author(s) 2026. CC BY 4.0 License.

Author	Model and case	Altitude range	What they simulate	Method used	TKE
MacDonald and Teixeira (2020)	1.5-order TKE closure model (steady-state single-column scheme); evaluated against CASES-99 tower data (surface layer, tower at 0–60 m)	0–0.5 km	Modelled steady-state TKE, stability functions (F_m, F_h), and turbulent Prandtl number	Analytical and numerical solution of the steady-state TKE budget with dual mixing lengths (l_m, l_h)	~ 0.003–$2.5\,\mathrm{m^2\,s^{-2}}$

Author contributions. NG wrote the code to conduct the analysis, analysed the results, and drafted the manuscript. IS, RW, and GB provided supervision and scientific insight and edited the text of the manuscript. TB and UA provided the model data and scientific insight and edited the manuscript. AB and YAM provided scientific insight and edited the manuscript. All authors reviewed and approved the final manuscript.

Competing interests. Gerd Baumgarten and Robin Wing are members of the editorial board of Atmospheric Measurement Techniques.

Acknowledgements. T.B. and U. A. thank the Deutsche Forschungsgemeinschaft (DFG, German Research Foundation) for partial support through CRC 301 "TPChange" (Project No. 428312742 and Projects B06 "Impact of small-scale dynamics on UTLS transport and mixing," B07 "Impact of cirrus clouds on tropopause structure," and Z03 "Joint model development and modelling synthesis"), and N.G., G.B., T.B., and U.A. thank DFG for support through the CRC 181 "Energy Transfers in Atmosphere and Ocean" (Project No. 274762653 and Projects W01 "Gravity-wave Parameterization for the Atmosphere" and S02 "Improved Parameterizations and Numerics in Climate Models") and the NATO Science for Peace and Security (SPS) Programme (grant no. G6122 MYP). I.S. was supported by the Federal Ministry for Economic Affairs and Climate Action based on a decision by the German Bundestag (DLR grant 50OE2301, project DEFINE). R.W. is supported by the AMILIS project funded by the Bundesministerium für Wirtschaft und Energie (BMWE, Federal Ministry for Economic Affairs and Energy) grant number 50 LZ 2503. Y.M. received support through Schmidt Sciences, LLC, as part of the Virtual Earth System Research Institute (VESRI). We thank Tom Dörffel for helpful scientific discussions.

https://doi.org/10.5194/egusphere-2026-6332
Preprint. Discussion started: 4 November 2026
© Author(s) 2026. CC BY 4.0 License.

References

Andrioli, V. F., Batista, P. P., Xu, J., Yang, G., Chi, W., and Zhengkuan, L.: Strong temperature gradients and vertical wind shear on MLT region associated to instability source at 23 S, Journal of Geophysical Research: Space Physics, 122, 4500–4511, https://doi.org/10.1002/2016JA023638, 2017.

Avsarkisov, V., Becker, E., and Renkwitz, T.: Turbulent parameters in the middle atmosphere: Theoretical estimates deduced from a gravity wave–resolving general circulation model, Journal of the Atmospheric Sciences, 79, 933–952, https://doi.org/10.1175/JAS-D-21-0005.1, 2022.

Banerjee, T., Kim, Y.-H., Voelker, G. S., Borchert, S., Kosareva, A., Kunkel, D., Masur, G.-T., Procházková, Z., Schmidli, J., and Achatz, U.: The impact of non-orographic gravity waves on transport and mixing: Effects of oblique propagation and coupling to turbulence, Journal of Geophysical Research: Atmospheres, 131, e2025JD045 270, https://doi.org/10.1029/2025JD045270, 2026.

Bašták Ďurán, I., Sakradzija, M., and Schmidli, J.: The two-energies turbulence scheme coupled to the assumed PDF method, Journal of advances in modeling earth systems, 14, e2021MS002 922, https://doi.org/10.1029/2021MS002922, 2022.

Baumgarten, G.: Doppler Rayleigh/Mie/Raman lidar for wind and temperature measurements in the middle atmosphere up to 80 km, Atmospheric Measurement Techniques, 3, 1509–1518, https://doi.org/10.5194/amt-3-1509-2010, 2010.

Blackadar, A. K.: The vertical distribution of wind and turbulent exchange in a neutral atmosphere, Journal of Geophysical Research, 67, 3095–3102, https://doi.org/https://doi.org/10.1029/JZ067i008p03095, 1962.

Borchert, S., Zhou, G., Baldauf, M., Schmidt, H., Zängl, G., and Reinert, D.: The upper-atmosphere extension of the ICON general circulation model (version: ua-icon-1.0), Geoscientific Model Development, 12, 3541–3569, https://doi.org/10.5194/gmd-12-3541-2019, 2019.

Bramberger, M., Dörnbrack, A., Wilms, H., Ewald, F., and Sharman, R.: Mountain-Wave Turbulence Encounter of the Research Aircraft HALO above Iceland, Journal of Applied Meteorology and Climatology, 59, 567–588, https://doi.org/10.1175/JAMC-D-19-0079.1, 2020.

Clayson, C. A. and Kantha, L.: On turbulence and mixing in the free atmosphere inferred from high-resolution soundings, Journal of Atmospheric and Oceanic Technology, 25, 833–852, https://doi.org/10.1175/2007JTECHA992.1, 2008.

Cohn, S. A.: Radar measurements of turbulent eddy dissipation rate in the troposphere: A comparison of techniques, Journal of Atmospheric and Oceanic Technology, 12, 85–95, https://doi.org/10.1175/1520-0426(1995)012<0085:RMOTED>2.0.CO;2, 1995.

Dehghan, A. and Hocking, W. K.: Instrumental errors in spectral-width turbulence measurements by radars, Journal of atmospheric and solar-terrestrial physics, 73, 1052–1068, https://doi.org/10.1016/j.jastp.2010.11.011, 2011.

Doms, G., Förstner, J., Heise, E., Herzog, H.-J., Mironov, D., Raschendorfer, M., Reinhardt, T., Ritter, B., Schrodin, R., Schulz, J.-P., and Vogel, G.: A Description of the Nonhydrostatic Regional COSMO-Model, Part II: Physical Parameterizations, COSMO Documentation Suite 6.00, Deutscher Wetterdienst, Offenbach, Germany, 2021.

Elvidge, A. D., Vosper, S. B., Wells, H., Cheung, J. C. H., Derbyshire, S. H., and Turp, D.: Moving towards a wave-resolved approach to forecasting mountain wave induced clear air turbulence, Meteorological Applications, 24, 540–550, https://doi.org/10.1002/met.1656, 2017.

Fiedler, J. and Baumgarten, G.: The ALOMAR Rayleigh/Mie/Raman lidar: status after 30 years of operation, Atmospheric Measurement Techniques, 17, 5841–5859, https://doi.org/10.5194/amt-17-5841-2024, 2024.

Fritts, D. C. and Alexander, M. J.: Gravity wave dynamics and effects in the middle atmosphere, Reviews of geophysics, 41, https://doi.org/10.1029/2001RG000106, 2003.

https://doi.org/10.5194/egusphere-2026-6332
Preprint. Discussion started: 4 November 2026
© Author(s) 2026. CC BY 4.0 License.

Gerding, M., Kopp, M., Höffner, J., Baumgarten, K., and Lübken, F.-J.: Mesospheric temperature soundings with the new, daylight-capable IAP RMR lidar, Atmospheric Measurement Techniques, 9, 3707–3715, https://doi.org/10.5194/amt-9-3707-2016, 2016.

Gerding, M., Wing, R., Franco-Diaz, E., Baumgarten, G., Fiedler, J., Köpnick, T., and Ostermann, R.: The Doppler wind, temperature, and aerosol RMR lidar system at Kühlungsborn, Germany–Part 1: Technical specifications and capabilities, Atmospheric Measurement Techniques, 17, 2789–2809, https://doi.org/10.5194/amt-17-2789-2024, 2024.

Goswami, N.: Data for: Quantifying turbulent kinetic energy in the middle atmosphere from wind and temperature observations, RADAR, https://www.radar-service.eu/radar/en/dataset/bufg4kh82d57jpyd?token=wsWfvFPIzRcgdLnShqpp, DOI to be provided by RADAR after acceptance, 2026a.

Goswami, N.: Reconstruction of UA-ICON Turbulent Kinetic Energy using wind and temperature data, https://doi.org/10.5281/zenodo.23298275, 2026b.

Grachev, A. A., Andreas, E. L., Fairall, C. W., Guest, P. S., and Persson, P. O. G.: The critical Richardson number and limits of applicability of local similarity theory in the stable boundary layer, Boundary-layer meteorology, 147, 51–82, https://doi.org/10.1007/s10546-012-9771-0, 2013.

Haack, A., Gerding, M., and Lübken, F.-J.: Characteristics of stratospheric turbulent layers measured by LITOS and their relation to the Richardson number, Journal of Geophysical Research: Atmospheres, 119, 10–605, https://doi.org/10.1002/2013JD021008, 2014.

He, Y., McFarlane, N., and Monahan, A. H.: A new TKE-based parameterization of atmospheric turbulence in the Canadian global and regional climate Models, Journal of Advances in Modeling Earth Systems, 11, 1153–1188, https://doi.org/10.1029/2018MS001532, 2019.

Hinze, J. O.: Turbulence, McGraw-Hill Series In Mechanical Engineering, McGraw-Hill, New York, http://isbnplus.org/9780070290372, 1975.

Hocking, W. K.: Measurement of turbulent energy dissipation rates in the middle atmosphere by radar techniques: A review, Radio Science, 20, 1403–1422, https://doi.org/10.1029/RS020i006p01403, 1985.

Hocking, W. K.: The dynamical parameters of turbulence theory as they apply to middle atmosphere studies, Earth, planets and space, 51, 525–541, https://doi.org/10.1186/BF03353213, 1999.

Holton, J. R. and Hakim, G. J.: An introduction to dynamic meteorology, vol. 88, Academic press, 2013.

Howard, L. N.: Note on a paper of John W. Miles, Journal of Fluid Mechanics, 10, 509–512, https://doi.org/10.1017/S0022112061000317, 1961.

Kaimal, J. C. and Finnigan, J. J.: Atmospheric boundary layer flows: their structure and measurement, Oxford university press, 1994.

Keckhut, P., Hauchecorne, A., and Chanin, M.-L.: A critical review of the database acquired for the long-term surveillance of the middle atmosphere by the French Rayleigh lidars, Journal of Atmospheric and Oceanic Technology, 10, 850–867, https://doi.org/10.1175/1520-0426(1993)010<0850:ACROTD>2.0.CO;2, 1993.

Khanna, J., Bandoro, J., Sica, R., and McElroy, C. T.: New technique for retrieval of atmospheric temperature profiles from Rayleigh-scatter lidar measurements using nonlinear inversion, Applied Optics, 51, 7945–7952, https://doi.org/10.1364/AO.51.007945, 2012.

Ko, H.-C., Chun, H.-Y., Geller, M. A., and Ingleby, B.: Global distributions of atmospheric turbulence estimated using operational high vertical-resolution radiosonde data, Bulletin of the American Meteorological Society, 105, E2551–E2566, https://doi.org/10.1175/BAMS-D-23-0193.1, 2024.

Kolmogorov, A. N.: Equations of turbulent motion in an incompressible fluid, in: Dokl. Akad. Nauk SSSR, vol. 30, pp. 299–303, https://cir.nii.ac.jp/crid/1571135650192651776, 1941.

https://doi.org/10.5194/egusphere-2026-6332
Preprint. Discussion started: 4 November 2026
© Author(s) 2026. CC BY 4.0 License.

Kolmogorov, A. N.: A refinement of previous hypotheses concerning the local structure of turbulence in a viscous incompressible fluid at high Reynolds number, Journal of Fluid Mechanics, 13, 82–85, https://doi.org/10.1017/S0022112062000518, 1962.

Kumar, M., Banerjee, T., Jonko, A., Mirocha, J., and Lassman, W.: Assessing the Turbulence Kinetic Energy Budget in the Boundary Layer Using WRF-LES: Impact of Momentum Perturbation, https://doi.org/10.5194/egusphere-egu21-13794, 2021.

Latteck, R., Singer, W., and Hocking, W. K.: Measurement of turbulent kinetic energy dissipation rates in the mesosphere by a 3 MHz Doppler radar, Advances in Space Research, 35, 1905–1910, https://doi.org/10.1016/j.asr.2005.06.056, 2005.

Liu, H.-L.: On the large wind shear and fast meridional transport above the mesopause, Geophysical Research Letters, 34, https://doi.org/10.1029/2006GL028789, 2007.

Lott, F. and Miller, M. J.: A new subgrid-scale orographic drag parametrization: Its formulation and testing in the ECMWF model, Quarterly Journal of the Royal Meteorological Society, 123, 101–127, https://doi.org/10.1002/qj.49712353704, 1997.

Lübken, F.-J.: Seasonal variation of turbulent energy dissipation rates at high latitudes as determined by in situ measurements of neutral density fluctuations, Journal of Geophysical Research: Atmospheres, 102, 13 441–13 456, https://doi.org/10.1029/97JD00853, 1997.

MacCready Jr, P. B.: Standardization of gustiness values from aircraft, Journal of Applied Meteorology and Climatology, 3, 439–449, https://doi.org/10.1175/1520-0450(1964)003<0439:SOGVFA>2.0.CO;2, 1964.

MacDonald, M. and Teixeira, J.: Scaling behavior of a turbulent kinetic energy closure scheme for the stably stratified atmosphere: A steady-state analysis, Journal of the Atmospheric Sciences, 77, 3161–3170, https://doi.org/10.1175/JAS-D-19-0332.1, 2020.

Mellor, G. L. and Yamada, T.: A hierarchy of turbulence closure models for planetary boundary layers, Journal of Atmospheric Sciences, 31, 1791–1806, https://doi.org/10.1175/1520-0469(1974)031<1791:AHOTCM>2.0.CO;2, 1974.

Mellor, G. L. and Yamada, T.: Development of a turbulence closure model for geophysical fluid problems, Reviews of Geophysics, 20, 851–875, https://doi.org/10.1029/RG020i004p00851, 1982.

Miles, J. W.: On the stability of heterogeneous shear flows, Journal of fluid Mechanics, 10, 496–508, https://doi.org/10.1017/S0022112061000305, 1961.

Morfa, Y. A., Stephan, C. C., Kunze, M., Siddiqui, T. A., Zülicke, C., Lehmacher, G., Mossad, M., Wing, R., Strelnikova, I., Baumgarten, G., Renkwitz, T., Urco, J. M., Latteck, R., Pautet, D., and Stolle, C.: Whole-atmosphere modeling with regional refinement: strengths and drawbacks assessed with observations from the VortEx campaign, Journal of Advances in Modeling Earth Systems, under review, 2026.

Nakanishi, M. and Niino, H.: Development of an improved turbulence closure model for the atmospheric boundary layer, Journal of the Meteorological Society of Japan. Ser. II, 87, 895–912, https://doi.org/10.2151/jmsj.87.895, 2009.

Nastrom, G. and Eaton, F.: Turbulence eddy dissipation rates from radar observations at 5–20 km at White Sands Missile Range, New Mexico, Journal of Geophysical Research: Atmospheres, 102, 19 495–19 505, https://doi.org/10.1029/97JD01262, 1997.

Nilsson, E., Lohou, F., Lothon, M., Pardyjak, E., Mahrt, L., and Darbieu, C.: Turbulence kinetic energy budget during the afternoon transition–Part 1: Observed surface TKE budget and boundary layer description for 10 intensive observation period days, Atmospheric Chemistry and Physics, 16, 8849–8872, https://doi.org/10.5194/acp-16-8849-2016, 2016.

Orr, A., Bechtold, P., Scinocca, J. F., Ern, M., and Janisková, M.: Improved middle atmosphere representation in the ECMWF forecast system through a new parameterization for non-orographic gravity waves, Journal of Climate, 23, 4905–4926, https://doi.org/10.1175/2010JCLI3490.1, 2010.

Prandtl, L.: Über ein neues Formelsystem für die ausgebildete Turbulenz, Nachrichten von der Akademie der Wissenschaften in Göttingen, Mathematisch-Physikalische Klasse, pp. 6–19, https://doi.org/10.1007/978-3-662-11836-8_72, reprinted in *Ludwig Prandtl Gesammelte Abhandlungen*, Springer, 1945.

https://doi.org/10.5194/egusphere-2026-6332
Preprint. Discussion started: 4 November 2026
© Author(s) 2026. CC BY 4.0 License.

Raschendorfer, M.: The new turbulence parameterization of LM, COSMO Newsletter, 1, 90–98, 2001.

Ratnam, M. V., Rao, D. N., Rao, T. N., Krishnaiah, M., Kumar, Y. B., Kumar, V. S., and Rao, P.: Coordinated MST radar and lidar observations for the study of mesospheric structures over a tropical station, Journal of atmospheric and solar-terrestrial physics, 64, 349–358, https://doi.org/10.1016/S1364-6826(01)00101-8, 2002.

Richardson, L. F.: The supply of energy from and to atmospheric eddies, Proceedings of the Royal Society of London. Series A, Containing Papers of a Mathematical and Physical Character, 97, 354–373, https://doi.org/10.1098/rspa.1920.0039, 1920.

Rüfenacht, R., Baumgarten, G., Hildebrand, J., Schranz, F., Matthias, V., Stober, G., Lübken, F.-J., and Kämpfer, N.: Intercomparison of middle-atmospheric wind in observations and models, Atmos. Meas. Tech., 11, 1971–1987, https://doi.org/10.5194/amt-11-1971-2018, 2018.

Satheesan, K. and Krishna Murthy, B.: Turbulence parameters in the tropical troposphere and lower stratosphere, Journal of Geophysical Research: Atmospheres, 107, ACL–2, https://doi.org/10.1029/2000JD000146, 2002.

Schneider, A., Wagner, J., Faber, J., Gerding, M., and Lübken, F.-J.: Case study of wave breaking with high-resolution turbulence measurements with LITOS and WRF simulations, Atmospheric Chemistry and Physics, 17, 7941–7954, https://doi.org/10.5194/acp-17-7941-2017, 2017.

Shao, J., Zhang, J., Wang, W., Zhang, S., Yu, T., and Dong, W.: Occurrence frequency of subcritical Richardson numbers assessed by global high-resolution radiosonde and ERA5 reanalysis, Atmospheric Chemistry and Physics, 23, 12 589–12 607, https://doi.org/10.5194/acp-23-12589-2023, 2023.

Sharman, R., Cornman, L., Meymaris, G., Pearson, J., and Farrar, T.: Description and derived climatologies of automated in situ eddy-dissipation-rate reports of atmospheric turbulence, Journal of applied meteorology and climatology, 53, 1416–1432, https://doi.org/10.1175/JAMC-D-13-0329.1, 2014.

Sherman, J. P. and She, C.-Y.: Seasonal variation of mesopause region wind shears, convective and dynamic instabilities above Fort Collins, CO: A statistical study, Journal of atmospheric and solar-terrestrial physics, 68, 1061–1074, https://doi.org/10.1016/j.jastp.2006.01.011, 2006.

Sica, R. J. and Haefele, A.: Retrieval of temperature from a multiple-channel Rayleigh-scatter lidar using an optimal estimation method, Applied optics, 54, 1872–1889, https://doi.org/10.1364/AO.54.001872, 2015.

Siri Jagan, R. and Schmidli, J.: Impact of model resolution and turbulence scheme on the representation of mountain waves and turbulence, Atmospheric Chemistry and Physics, 26, 13 721–13 741, https://doi.org/10.5194/acp-26-13721-2026, 2026.

Söder, J., Zülicke, C., Gerding, M., and Lübken, F.-J.: High-resolution observations of turbulence distributions across tropopause folds, Journal of Geophysical Research: Atmospheres, 126, e2020JD033 857, https://doi.org/10.1029/2020JD033857, 2021.

Strelnikov, B., Rapp, M., and Lübken, F.-J.: A new technique for the analysis of neutral air density fluctuations measured in situ in the middle atmosphere, Geophysical research letters, 30, https://doi.org/10.1029/2003GL018271, 2003.

Strelnikov, B., Szewczyk, A., Strelnikova, I., Latteck, R., Baumgarten, G., Lübken, F.-J., Rapp, M., et al.: Spatial and temporal variability in MLT turbulence inferred from in situ and ground-based observations during the WADIS-1 sounding rocket campaign, Annales Geophysicae, 35, 547–565, https://doi.org/10.5194/angeo-35-547-2017, 2017.

Strelnikov, B., Rapp, M., Lübken, F.-J., Schüler, K., Baumgarten, G., Strelnikova, I., and Wing, R.: High latitude mesospheric turbulence measured in-situ since 1990, Journal of Geophysical Research: Atmospheres, submitted, 2026.

Stull, R. B.: An Introduction to Boundary Layer Meteorology, Springer Netherlands, https://doi.org/10.1007/978-94-009-3027-8, 1988.

https://doi.org/10.5194/egusphere-2026-6332
Preprint. Discussion started: 4 November 2026
© Author(s) 2026. CC BY 4.0 License.

Theuerkauf, A., Gerding, M., and Lübken, F.-J.: LITOS–a new balloon-borne instrument for fine-scale turbulence soundings in the stratosphere, Atmospheric Measurement Techniques, 4, 55–66, https://doi.org/10.5194/amt-4-55-2011, 2011.

Tkachenko, E. V., Debolskiy, A. V., and Mortikov, E. V.: Analysis of turbulent kinetic energy decay power law in atmospheric boundary layer models, IOP Conference Series: Earth and Environmental Science, 611, 012 014, https://doi.org/10.1088/1755-1315/611/1/012014, 2020.

Voelker, G. S., Bölöni, G., Kim, Y.-H., Zängl, G., and Achatz, U.: MS-GWaM: A Three-Dimensional Transient Gravity Wave Parametrization for Atmospheric Models, Journal of the Atmospheric Sciences, 81, 1181 – 1200, https://doi.org/10.1175/JAS-D-23-0153.1, 2024.

von Zahn, U., von Cossart, G., Fiedler, J., Fricke, K. H., Nelke, G., Baumgarten, G., Rees, D., Hauchecorne, A., and Adolfsen, K.: The ALOMAR Rayleigh/Mie/Raman lidar: objectives, configuration, and performance, Annales Geophysicae, 18, 815–833, https://doi.org/10.1007/s00585-000-0815-2, 2000.

Wing, R., Hauchecorne, A., Keckhut, P., Godin-Beekmann, S., Khaykin, S., McCullough, E. M., Mariscal, J.-F., and d'Almeida, E.: Lidar temperature series in the middle atmosphere as a reference data set–Part 1: Improved retrievals and a 20-year cross-validation of two co-located French lidars, Atmospheric Measurement Techniques, 11, 5531–5547, https://doi.org/10.5194/amt-11-5531-2018, 2018.

Wing, R., Strelnikova, I., Dörnbrack, A., Gerding, M., Franco-Diaz, E., Holt, L., Mossad, M., and Baumgarten, G.: Direct observation of quasi-monochromatic gravity wave packets associated with the polar night jet using a Doppler-Rayleigh LiDAR, Journal of Geophysical Research: Atmospheres, 130, e2025JD043 707, https://doi.org/10.1029/2025JD043707, 2025.

Woodman, R. F. and Guillen, A.: Radar observations of winds and turbulence in the stratosphere and mesosphere, Journal of Atmospheric Sciences, 31, 493–505, https://doi.org/10.1175/1520-0469(1974)031<0493:ROOWAT>2.0.CO;2, 1974.

Xian, J., Qiu, Z., Luo, H., Hu, Y., Lin, X., Lu, C., Yang, Y., Yang, H., and Zhang, N.: Turbulent energy budget analysis based on coherent wind lidar observations, Atmospheric Chemistry and Physics, 25, 441–457, https://doi.org/10.5194/acp-25-441-2025, 2025.

Yang, F. and Liu, A. Z.: Stability characteristics of the mesopause region above the Andes, Journal of Geophysical Research: Space Physics, 127, e2022JA030 315, https://doi.org/10.1029/2022JA030315, 2022.

Zängl, G., Reinert, D., Rípodas, P., and Baldauf, M.: The ICON (ICOsahedral Non-hydrostatic) modelling framework of DWD and MPI-M: Description of the non-hydrostatic dynamical core, Quarterly Journal of the Royal Meteorological Society, 141, 563–579, https://doi.org/10.1002/qj.2378, 2015.